

IMPACT ABSORBING LATTICE STRUCTURES PRODUCED BY ADDITIVE
MANUFACTURING

A THESIS SUBMITTED TO
THE GRADUATE SCHOOL OF NATURAL AND APPLIED SCIENCES
OF
MIDDLE EAST TECHNICAL UNIVERSITY

BY

ROOZBEH NESHANI

IN PARTIAL FULFILLMENT OF THE REQUIREMENTS
FOR
THE DEGREE OF MASTER OF SCIENCE
IN
MECHANICAL ENGINEERING

JANUARY 2022

Approval of the thesis:

**IMPACT ABSORBING LATTICE STRUCTURES PRODUCED BY
ADDITIVE MANUFACTURING**

submitted by **ROOZBEH NESHANI** in partial fulfillment of the requirements for
the degree of **Master of Science in Mechanical Engineering, Middle East
Technical University** by,

Prof. Dr. Halil Kalıpçılar
Dean, Graduate School of **Natural and Applied Sciences** _____

Prof. Dr. M. A. Sahir Arıkan
Head of the Department, **Mechanical Engineering** _____

Assoc. Prof. Dr. Sezer Özerinç
Supervisor, **Mechanical Engineering, METU** _____

Examining Committee Members:

Assoc. Prof. Dr. Ulaş Yaman
Mechanical Eng., METU _____

Assoc. Prof. Dr. Sezer Özerinç
Mechanical Eng., METU _____

Prof. Dr. Bahattin Koç
Engineering and Natural Sciences, Sabancı Üniversitesi _____

Assoc. Prof. Dr. Hüsnü Dal
Mechanical Eng., METU _____

Assoc. Prof. Dr. Ender Yıldırım
Mechanical Eng., METU _____

Date: 10.01.2022

I hereby declare that all information in this document has been obtained and presented in accordance with academic rules and ethical conduct. I also declare that, as required by these rules and conduct, I have fully cited and referenced all material and results that are not original to this work.

Name Last Name : Roozbeh Neshani

Signature :

ABSTRACT

IMPACT ABSORBING LATTICE STRUCTURES PRODUCED BY ADDITIVE MANUFACTURING

Neshani, Roozbeh
Master of Science, Mechanical Engineering
Supervisor : Assoc. Prof. Sezer Özerinç

January 2022, 83 pages

Recent technological advances rendered additive manufacturing (AM) a disruptive technology for the development and manufacturing of next generation complex parts and lightweight structures. AM of polymeric parts is widely applicable to structural parts ranging from load bearing components to impact absorbing structures. Digital Light Synthesis (DLS) is a recently developed technique that enables the reliable, fast and accurate AM of a wide range of polymeric materials. DLS is especially effective in producing lattice parts – three-dimensional open-cell structures composed of repeating unit cells. This thesis investigates elastomeric polyurethane (EPU) lattice parts produced by DLS and characterizes their mechanical properties. Initial characterization of fully dense EPU demonstrated the nonlinear hyperelastic behavior of this material combined with high elongation at fracture and excellent recovery. A combination of Ogden model and Prony series successfully described the visco-hyperelastic behavior. Next, octet-truss, BCC+CP, and cubic type lattice structures were produced and their energy absorption performances under quasi-static compression were characterized. In general, Octet-truss structures provided a more reliable and effective architecture for absorbing energy due to the balancing

effects of buckling and stretching. Accurate control of the truss diameter provided means for tuning the peak stress and energy absorbance capacity of the lattice geometries for the requirements of a wide range of applications. Overall, the findings demonstrated the great potential of the EPU and the DLS technique for the design and implementation of energy-absorbing structures.

Additionally, through combining the excellent capabilities of DLS 3D printing method and another type of resin, namely the rigid polyurethane RPU 70, with a novel approach of depositing NiCo (Nickel, Cobalt) metallic alloy, the feasibility of hybrid production of metal-polymer lattice structures was demonstrated. Metal plated polymer honeycomb structure exhibited orders of magnitude increase in compression strength.

Keywords: Digital Light Synthesis, Electroplating, Additive Manufacturing, Lattice Structures, Energy Absorption

ÖZ

DARBE EMİCİ KAFES YAPILARIN EKLEMELİ İMALAT YÖNTEMİYLE ÜRETİMİ

Neshani, Roozbeh
Yüksek Lisans, Makina Mühendisliği
Tez Yöneticisi: Doç. Dr. Sezer Özerinç

Ocak 2022, 83 sayfa

Son teknolojik gelişmeler, katmanlı üretimi, yeni nesil karmaşık parçaların ve hafif yapıların geliştirilmesi ve üretimi için çığır açan bir teknoloji haline getirdi. Polimerik parçaların katmanlı imalatı, yük taşıyan bileşenlerden darbe emici yapılara kadar uzanan yapısal parçalara geniş ölçüde uygulanabilir. Dijital Işık Sentezi (DLS), çok çeşitli polimerik malzemelerin güvenilir, hızlı ve doğru Eklemeli Üretimini sağlayan yeni geliştirilmiş bir tekniktir. DLS özellikle kafes parçalarının, tekrar eden birim hücrelerden oluşan üç boyutlu açık hücreli yapıların üretilmesinde etkilidir. Bu tez, DLS tarafından üretilen elastomerik poliüretan (EPU) kafes parçalarını incelemekte ve mekanik özelliklerini karakterize etmektedir. Tamamen yoğun EPU'nun ilk karakterizasyonu, yüksek kopma uzama oranı ve mükemmel deformasyon geri kazanımı ile birlikte bu malzemenin doğrusal olmayan hiperelastik davranışını gösterdi. Ogden modeli ve Prony serisinin bir kombinasyonu, visko-hiperelastik davranışı başarıyla tanımladı. Daha sonra oktet-kafes, BCC+CP ve kübik tip kafes yapılar üretilmiş ve yarı statik sıkıştırma altında enerji emici performansları karakterize edilmiştir. Genel olarak Octet kafes yapılar, burkulma ve esnemenin dengeleyici etkilerinden dolayı enerjiyi emmek için daha güvenilir ve etkili bir mimari sağlamıştır. Dikme çapının doğru kontrolü, çok çeşitli

uygulamaların gereksinimleri için kafes geometrilerinin peak gerilimi ve enerji emme kapasitesinin ayarlanması için çözümler sağladı. Genel olarak, bulgular, enerji emici yapıların tasarımı ve uygulanması için EPU ve DLS tekniğinin büyük potansiyelini gösterdi. Ayrıca, DLS 3D baskı yönteminin mükemmel özellikleri ve diğer bir reçine türü olan rijit poliüretan RPU 70 kullanarak, ve NiCo (Nikel, Kobalt) metalik alaşımını yeni bir kaplama yaklaşımı ile birleştirerek, metal-polimer kafes yapılarının hibrit üretim imkanı gösterildi. Metal kaplı polimer petek yapısı, sıkıştırma mukavemetinde büyük artışlar sergiledi.

Anahtar Kelimeler: Dijital Işık Sentezi, Eklemeli İmalat, Elektrokaplama, Kafes Yapılar, Enerji Emicilik

*to my beloved family who have been supportive all my life and
encouraged me to pursue my academic career.*

ACKNOWLEDGMENTS

The author wishes to express his deepest gratitude to his supervisor Assoc. Prof. Sezer Özerinç for his guidance, advice, criticism, encouragements, and insight throughout the research.

The author would also like to thank our collaborators Prof. Dr. William P. King, and Assoc. Prof. Dr. Sameh Tawfick from UIUC, USA for their constructive suggestions and Fast Radius Inc., USA, for providing the testing materials.

The technical assistance of Mr. Servet Şehirli, Mr. Ali Güzel are gratefully acknowledged.

Finally, the author would like to thank the current and alumni members of the Nanomechanics laboratory, Burçin Kaygusuz, Mehmet Kepenekçi, and Ali Bagheri for their assistance and encouragement.

TABLE OF CONTENT

ABSTRACT.....	v
ÖZ.....	vii
ACKNOWLEDGMENTS	x
TABLE OF CONTENT	xi
LIST OF TABLES	xiv
LIST OF FIGURES	xv
LIST OF ABBREVIATIONS	xviii
CHAPTERS	
1 INTRODUCTION	1
1.1 Additive Manufacturing.....	1
1.2 Lattice Structures	3
1.2.1 Lattice Structure Types and Design methods.....	6
1.3 Continuous Liquid Interface Production (CLIP)	8
1.4 Part 1: Elastomeric Polyurethane Lattice Structures.....	9
1.5 Part 2: NiCo/RPU composite honeycomb lattice structure.....	10
1.5.1 A hybrid approach combining metal electroplating of polymer lattices ...	10
1.5.2 Drawbacks of Electroless Plating of Non-Conductive Polymers.....	11
1.5.3 Remarks on the merits of the hybrid production approach and parts selection.	12
1.5.4 Other applications of metallizing polymers.	14
2 PART 1.1: ELASTOMERIC PARTS PRODUCED BY DLS FOR MATERIAL CHARACTERIZATION	15

2.1	Experiment	15
2.2	Tensile Test Results.....	19
2.2.1	Modeling of the Hyperelastic Response	21
2.3	Stress Relaxation Test Results.....	25
2.4	Further discussion on the hyperelastic and viscoelastic models	29
2.5	Dynamic Mechanical Analysis Results	31
3	PART 1.2: ELASTOMERIC LATTICE STRUCTURE PARTS PRODUCED BY DLS	35
3.1	Design and Preparation of the Lattice Parts	35
3.2	Lattice Compression Test Results	38
3.3	Effect of Slenderness Ratio on the Performance Metrics.....	45
3.4	Comparison of the performance of all the lattice structure types.....	48
4	PART 2: A METHODOLOGY TO DEVELOP METAL-COATED POLYMER LATTICES	51
4.1	Hybrid Production Process	51
4.2	Rigid Polyurethane honeycomb lattice structure.....	52
4.3	The Electroless Copper Plating process	54
4.4	NiCo Electroplating process.....	55
4.5	Coating Thickness	57
4.6	Compression test on the coated samples	58
4.7	Failure mechanism.....	62
5	CONCLUSIONS AND FUTURE WORK.....	65
5.1	Conclusions	65
5.2	Future work	66

REFERENCES69

LIST OF TABLES

TABLES

Table 2.1 A summary of specimen types and tests employed.....	16
Table 2.2. Constants of the curve fit for 2-term Ogden and Neo Hookean hyperelastic models.	24
Table 2.3. Prony series constants obtained after fitting the model to experimental results.....	28
Table 3.1 Summary of the lattice parts produced and some key parameters.	37
Table 3.2. Summary of the quasi-static compression test results for different lattice structures.....	45
Table 4.1. Thickness of the coated samples and the duration of the electroplating process (the electroplating process involved turning the sample inside the setup upside down after half the duration of the coating was reached).	57
Table 4.2. Summary of the compression test results for apparent elastic modulus and yield stress.	60

LIST OF FIGURES

FIGURES

Figure 1.1. Development of 3D printing methods over the span of 30 years(Jakus 2019).	3
Figure 1.2 Comparison between energy absorption performance of foams and elastomeric lattice structures (Clough et al. 2019).....	5
Figure 1.3 Number of different lattice structures studied in the literature(Helou and Kara 2018).	7
Figure 1.4 Schematics of the CLIP process.	9
Figure 1.5 Electroless deposition rate of Cu using different activation solutions. The Deposition rate is impractical for high thickness coatings(Vaškėlis et al. 1997).	12
Figure 2.1 (a) Dimensions of the ASTM D412 specimen type A. (b) A photograph of a printed Type A specimen. (c) A photograph of the tensile testing setup. (d) Photograph of a printed cylindrical specimen with its dimensions. (e) Photograph of the compressive relaxation test setup.	17
Figure 2.2. (a) Engineering stress vs. engineering strain behavior of EPU 41 under uniaxial tension. The data reported by the manufacturer is provided for comparison. The dashed lines show the predictions of Neo Hookean and Ogden models. (b) Data shown for small strains.....	20
Figure 2.3. Stress vs. Strain data for EPU 41 from tensile experiment on a Type A specimen, fitting curve obtained from 2-term Ogden and Neo-Hookean Models, and the data provided from the manufacturer.	24
Figure 2.4. (a) Stress relaxation behavior of EPU 41 after rapid tensile loading. Dashed lines show the predictions of the visco-hyperelastic model. (b) Relaxation modulus variation for the whole duration of the experiment. Inset shows the normalized stress, σ / σ_0 , vs. time.	26

Figure 2.5. Representation of Generalized Maxwell model, employing a series of spring-dashpot elements for viscosity and time dependent behavior of materials (A. Alperen Bakır, Neshani, and Özerinç 2021)27

Figure 2.6. (a) 48-hour stress relaxation response under compression. The dashed line indicates the Prony series fit. (b) The corresponding load vs. displacement data, showing 13% compression set upon unloading. (c) The corresponding load vs. time data.....29

Figure 2.7. temperature sweep test result from DMA test compared to the data provided by the vendor for EPU 41.....32

Figure 2.8. (a) Frequency sweep test results from multiple DMA tests. (b) glass transition temperature’s shift trend with relation to loading frequency.33

Figure 3.1. The solid models of each unit cell type, photographs of printed specimens, and photographs of the test setup. The truss length is a , and the truss diameter is d36

Figure 3.2. (a) Force vs. displacement response of a Cubic 2 sample for four different strain targets. (b) Stress-strain behavior and the efficiency of the lattice as a function of strain. (c) Corresponding energy diagram of the lattice under compression. (d) Snapshots from the test footage at different strains.....39

Figure 3.3 (a) Force vs. displacement response of an Octet 1 sample for four different strain targets. (b) Stress-strain behavior and the efficiency of the lattice as a function of strain. (c) Corresponding energy diagram of the lattice under compression. (d) Snapshots from the test footage at different strains.....43

Figure 3.4 (a) Force vs. displacement response of a BCC + CP 2 sample for four different strain targets. (b) Stress-strain behavior and the efficiency of the lattice as a function of strain. (c) Corresponding energy diagram of the lattice under compression. (d) Snapshots from the test footage at different strains.....44

Figure 3.5. Effect of slenderness ratio on a wide range of compressive performance metrics for Cubic, BCC+CP, and Octet lattice structures.48

Figure 3.6 (a) Normalized energy diagrams of lattice structures for different types and strut diameters. The number on each curve is the strut diameter of each sample

in mm. (b) Normalized compressive stress-strain behavior of the samples investigated in this work.	50
Figure 4.1. Image of a virgin uncoated RPU 70 honeycomb lattice structure next to post-mortem electroplated samples.....	52
Figure 4.2. Tensile test results of RPU 70 in accordance with ASTM D638 standard with 500 mm/min loading speed.....	53
Figure 4.3. (a) A regular hexagonal unit cell of honeycomb structure with a wall thickness of 0.5 mm. (b) Isometric view of the CAD design for the lattice structure with 68 hexagons. The in-plane and out-of-plane directions as well as the overall dimensions of the part are shown in this figure.	53
Figure 4.4. Electrolytic unit cell setup. The indicated yellow parts are the setup assembly parts that were 3D printed from PLA/PHA. The blue colored part is the stainless-steel plate that has the accurate hexagonal cutout pattern so it could fit snugly within the spaces between the protrusions.	56
Figure 4.5. Picture taken from the compression test setup.	58
Figure 4.6. Compression test results of coated and uncoated samples up to yield point. Per standard, the yield point is the maximum exhibited stress for the structures that fail within 10% of strain.....	59
Figure 4.7. summary of the compression test findings that indicate existence of a trend attributed to the thickness of the deposited metal coating.....	61
Figure 4.8. Snapshots from the footage of compression tests on (a) uncoated (b) 47 microns coated (c) 97 microns coated and (d) 87 microns coated samples.....	63

LIST OF ABBREVIATIONS

ABBREVIATIONS

AM – Additive Manufacturing

3D – Three dimensional

EPU – Elastomeric Polyurethane

CLIP – Continuous Liquid Interface Production

DLS – Digital Light Synthesis

RPU – Rigid Polyurethane

SLA – Stereolithography

DMA – Dynamic Mechanical Analysis

ASTM – American Society for Testing and Materials

FFF – Fused Filament Fabrication

SLM – Selective Laser Melting

CHAPTER 1

INTRODUCTION

1.1 Additive Manufacturing

Traditional manufacturing methods mostly revolve around subtractive techniques where a block of the raw material is reshaped by special tools or in other cases are based on molding and forging. The straightforwardness and low-cost aspects of such methods allowed industries to extensively use them. Concurrently, the materials used in the mainstream industry have been continuously studied and examined to achieve higher performance in various applications namely, mechanical, and structural, heat transfer, electronics, and more. As new materials with exceptional properties are developed to become much stiffer and resistant to extreme loads and conditions, the structural design of the parts also shifts towards highly optimized and better performance to weight geometries. Often, such designs are very costly or impossible to manufacture by traditional methods because of both the limitations of the subtractive methods and the ever-increasing difficulty of processing extremely hard and strong new materials (machinability) (Ngo et al. 2018). Additive manufacturing (AM) is a technology that enables the production of structural parts in a layer-by-layer approach. Recent advances in a wide range of AM technologies have

transformed this manufacturing paradigm from a mere rapid prototyping tool to a rapidly evolving industry that offers versatile and novel solutions for automotive, aerospace, defense, consumer product, and packaging applications (Thompson et al. 2016)(Dilberoglu et al. 2017). Over the span of nearly 40 years, different techniques have been introduced to increase the production rate (printing speed) or tackle the inherited defects of the printed parts due to material properties or printing methods. Stereolithography (SLA) was introduced in 1983 as one of the primary photopolymerization techniques and consequently other 3D printing methods such as Digital Light Processing (DLP) (Yaman et al. 2017), vat photopolymerization (Bagheri and Jin 2019), Fused Filament Fabrication (FFF) (Ali Alperen Bakır, Atik, and Özerinç 2021; A. Alperen Bakır, Neshani, and Özerinç 2021), Direct Energy Deposition (DED) (Natarajan 2021), etc., evolved over the next years. Figure 1.1. demonstrates a demographic of the developments in AM in recent years(Jakus 2019).

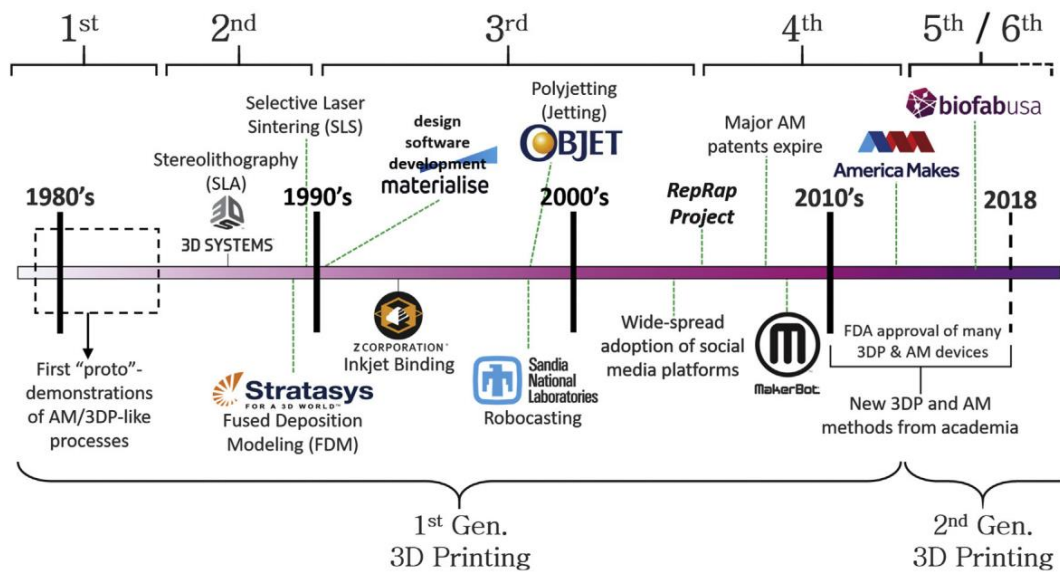


Figure 1.1. Development of 3D printing methods over the span of 30 years(Jakus 2019).

1.2 Lattice Structures

The advances in AM have also rendered the production of a wide range of novel material architectures feasible. Some examples include lattice structures (Nazir et al. 2019), functionally graded materials (C. Zhang et al. 2019), and topologically optimized components (Liu et al. 2018). Among these, lattice structures are lightweight materials composed of a periodic arrangement of trusses in a specific configuration. Lattice structures have low density and high impact energy absorbance performance. The cell geometry provides a vast design space for tuning the structure's properties for meeting the specific requirements of any application. All these advantages make lattice structures promising for a wide range of applications.

Previous studies provided a thorough understanding of the complex mechanical behavior of lattice structures (L. J. Gibson and Ashby 1997). However, the challenges in their manufacturing have limited the implementation of the technology for decades. As a result of the advancements in AM technology that enable the generation of complex structures, lattice structures have become a widely studied topic once again to realize their full potential in industrial applications (Montgomery et al. 2020).

AM can produce lattice structures made of metals, ceramics, and polymers. Main applications involve the design, development, and manufacturing of lightweight structural components (Plocher and Panesar 2019), biomedical implants (Mahmoud and Elbestawi 2017), and impact energy-absorbing structures (Davami et al. 2019; Ha and Lu 2020; Xu, Zhang, and Zhang 2018). Lattice structures made of elastomer polymers exhibit excellent compliance and recovery, making them valuable architectures for designing new generation impact-absorbing structures. Recent studies towards this objective range from fundamental studies probing the mechanics of AM-produced elastomers (A. Alperen Bakır, Neshani, and Özerinç 2021; Meem et al. 2021; Hossain, Navaratne, and Perić 2020; Abayazid and Ghajari 2020; Moore and Williams, n.d.) to the design and implementation of new generation helmets (Clough et al. 2019), force-sensing soft grippers for robotic arms (Dilibal et al. 2021), and self-healing elastomers for biomedical devices (Yu et al. 2019).

A recent study (Clough et al. 2019) demonstrated that elastomeric lattice structures can perform with similar efficiency of conventional foams. Foams are the prominent porous type of material that is used to produce protective gears such as helmets. Two

major drawbacks of using foams are that under consecutive impacts the foams lose their initial capacity and are not able to absorb the target energy threshold especially in the cases of higher applied stresses. Elastomer lattices, due to the resilient properties of them can maintain their performance, are much better suited for application that require a steady performance for example: sportswear and shoes. Second drawback of foams is that the stochastic distribution of the cavities makes it impossible to change the mechanical response via porosity the only possible way is to control the mean volume of the gaps and not how they are sealed. Lattice structures offer a diverse solution for fine tuning the structure per need with even higher porosity levels and better performance to weight ratio. Taken from the literature, Figure 1.2 compares the efficiency of lattice structures and foams, supporting the idea that elastomeric lattices are a much better solution for cases that require higher stress tolerance.

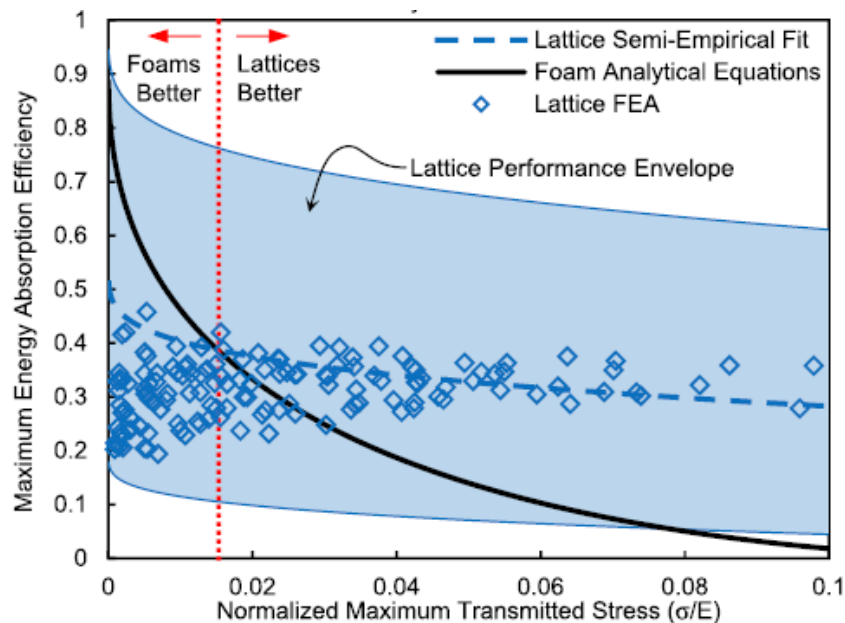


Figure 1.2 Comparison between energy absorption performance of foams and elastomeric lattice structures (Clough et al. 2019).

1.2.1 Lattice Structure Types and Design methods

Lattice structures can be classified according to their core unit cell types and how they are configured next to each other (Pan, Han, and Lu 2020; Helou and Kara 2018). One of the most studied and prominent families of lattice structures is the cubic type. In that, various arrangements of struts compose the unit cells. To name a few, simple cubic, Octet truss, Face Centered Cubic (FCC), and body centered cubic unit cells and their combinations are among the most studied structures. The unit cells are usually arranged in three-dimensional orientation with common struts for the adjacent ones. Diamond, Tetrahedral are the less common types of basic lattice structures. More complex geometries such as Voronoi diagram based structures has also been studied extensively (Stanković and Shea 2020). Furthermore, for the structures that expand the unit cells only in two dimensions as in-plane, hexagonal honeycomb structure is one of the most successful and established types. In addition, circular, tetragonal, auxetic lattices also fall under this type (Kona et al. 2021; P. Zhang, Arceneaux, and Khattab 2018; Habib et al. 2018a; 2017). These in-plane expanded structures are extensively used for their excellent crashworthiness especially for the applications that implement them in a sandwich like manner between two plates. Figure 1.3, shows how many studies used various lattice structure for their study. It can be seen that the cubic family structures have been studied broadly and it is one of the main reasons that this study selected BCC+CP, Octet truss, and cubic structures for the second chapter.

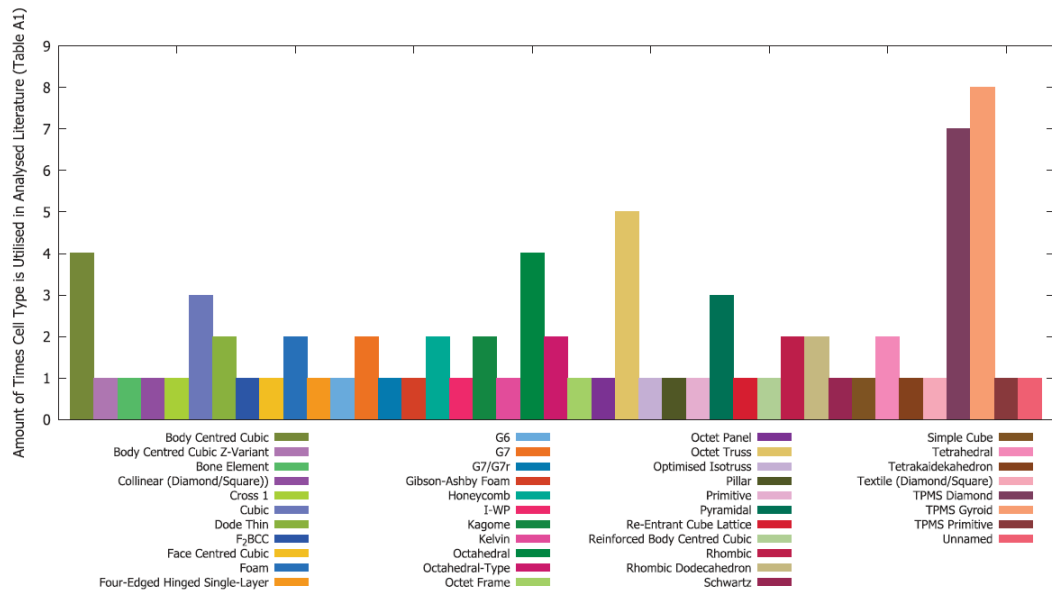


Figure 1.3 Number of different lattice structures studied in the literature(Helou and Kara 2018).

Designing lattice structures, primarily depends on the main approach. For the cubic case, a basic wireframe approach is sufficient to produce the mainframe of the unit cell. The struts revolve around the main body frame with select cross section design (in this study circular). Other approaches to produce lattice structures are available as well, namely, using spatial equations to produce the planes that form the lattice, and using topology optimization with appropriate boundary restraints like relative density or stress distribution (Pan, Han, and Lu 2020; Helou and Kara 2018; Thompson et al. 2016; Beyer and Figueroa 2016). While the former approach is much easier to follow, the intrinsic properties of the lattice structures remain intact. However, latter approach allows for a broader option regarding fine tuning the unit cells even individually as has been observed in the literature for the cases that study functionally graded lattice structures

There are various design tools to prepare the geometries in CAD environment. For the simple wireframe-based lattices any conventional CAD tool is sufficient. However, designing a much sophisticated and by large number of unit cells requires more specialized tools. nTopology, and Autodesk (“Fusion 360 with Netfabb” n.d.; “NTop; Next-Generation Engineering Design Software” n.d.) companies provide software capable of designing such complex structures, to name a few. In this work the vendor has developed a cloud base software, Carbon Design Engine (“Carbon Design Engine” n.d.), that easily produces the geometries. In this work’s case, a simple cubic prism was set to be filled with the unit cells with desired dimensions.

1.3 Continuous Liquid Interface Production (CLIP)

One recently developed technology for the AM of polymeric materials is Continuous Liquid Interface Production (CLIP) (Tumbleston et al. 2015), DLS is an improved version of stereolithography (SLA), a VAT photopolymerization-based 3D printing method. The main difference of DLS is the incorporation of a dead zone between the curing layer and the bottom window of the resin tank. This novel approach eliminates the separation step of the build platform from the window for each layer. As a result, a continuous curing process is achieved that offers at least an order of magnitude faster production rates than conventional SLA (Bagheri and Jin 2019; Pagac et al. 2021; Januszewicz et al. 2016). The continuous curing scheme reduces the

mechanical anisotropy commonly encountered in other AM methods (Ali Alperen Bakır, Atik, and Özerinç 2021). Furthermore, the approach does not require support structures for most cases and provides high resolution down to 30 micron while maintaining a high level of repeatability (McGregor, Tawfick, and King 2019b). All these advantages make DLS an excellent technique for manufacturing lattice parts for industrial applications and mass production.

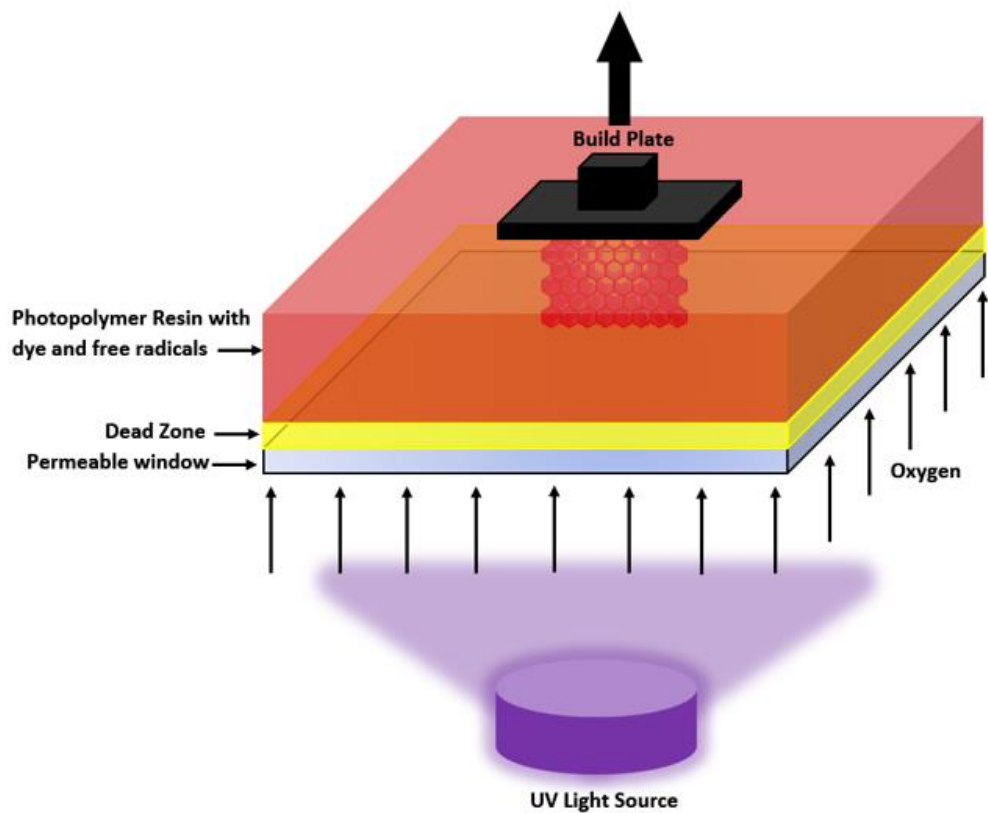


Figure 1.4 Schematics of the CLIP process.

1.4 Part 1: Elastomeric Polyurethane Lattice Structures

In the first part of the study, we explore the capabilities of DLS through a recently developed high-performance elastomer material, EPU 41. We first characterize the

basic mechanical behavior of the elastomer through standard mechanical testing and then produce a range of lattice structures and investigate their impact absorbance performance under compression.

1.5 Part 2: NiCo/RPU composite honeycomb lattice structure

The second part of this work investigates honeycomb lattice structures manufactured by a combination of Electroless/Electroplated NiCo alloy on DLS 3D printer rigid polymer. The main focus of the study is to showcase the feasibility of producing impact absorbing metal/polymer composite protective structures with comparable performance to their metal counterparts.

1.5.1 A hybrid approach combining metal electroplating of polymer lattices

Electroless and subsequently electroplating metals over 3D printed polymer-based parts is a hybrid manufacturing process that leads to the production of parts that are highly optimized (i.e., topological, thermal, etc.) through AM while concurrently benefiting from the consequent coating of the additional metals(Garcia et al. 2010; Yabu, Hirai, and Shimomura 2006; Angel et al. 2018a). The metal coating can increase the structural stiffness of the part and provide sufficient conductivity so that the parts can be used in applications such as radio transmission like large-scale antennae or even small structures such as smartphones and other electronic devices(Jiang et al. 2018; Ruskova et al. 2018; 2018). Furthermore, the elevated mechanical capacity of coated lattice structure parts makes them a viable option for

moderate to high impact energy absorption applications(Song et al. 2018). In the final chapter of this study, we explore the feasibility of combining DLS 3D printing method, and metal electroplating to produce metallized honeycomb lattice structures that exhibit better structural and impact absorbing performance.

1.5.2 Drawbacks of Electroless Plating of Non-Conductive Polymers

There are various methods for metallization of polymers such as physical vapor deposition (PVD)(Juarez et al. 2018), brushing (Jiang et al. 2018), and Electroless plating of non-conductive polymers which is a process that involves meticulous preparation steps. The polymer part, after surface preparation and activation, is submerged inside a bath of the electrolyte made from the common ionic salts of the to be coated metal. the coating process is straightforward in the sense that an electrolytic cell is created via placing plates of pure coating metal as anodes inside the bath in the proximity of the part. A constant voltage ensures a steady current that is necessary for the metal atoms to get attached on the surface of the part. Contamination and oxidation free environment will ensure a homogenic coating surface. However, the chemicals that are required for the activation are highly toxic and environmentally hazardous(Eßbach, Fischer, and Nickel 2021; Tengsuwan and Ohshima 2014; Wang et al. 2011). Furthermore, the deposition rate of electroless process is considerably slow which renders it, for coating higher thicknesses, impractical as demonstrated in Figure 1.5 (Vaškėlis et al. 1997). Therefore, direct electroplating is a much faster method in comparison and since it is only viable once

the part is conductive the combination of the two plating methods is the solution for achieving higher thicknesses.

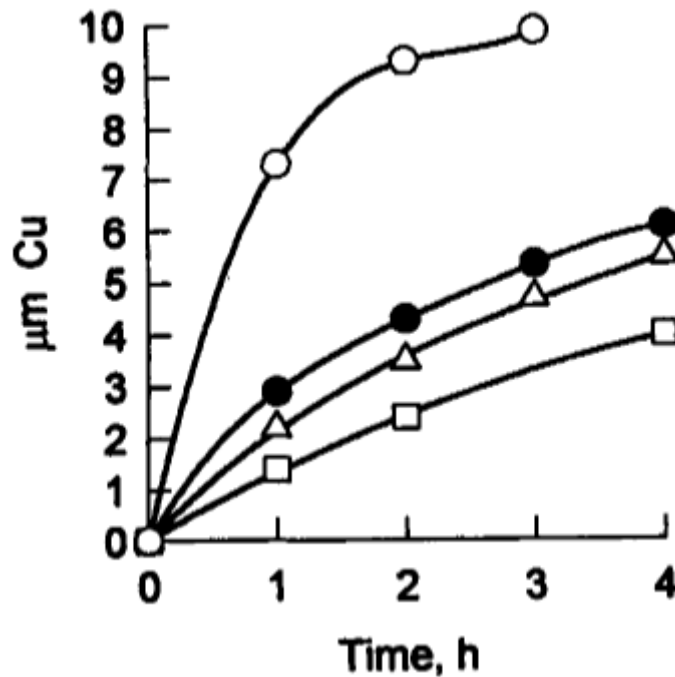


Figure 1.5 Electroless deposition rate of Cu using different activation solutions. The Deposition rate is impractical for high thickness coatings(Vaškėlis et al. 1997).

1.5.3 Remarks on the merits of the hybrid production approach and parts selection.

Metal AM can produce lattice structures for lightweight structural and protective applications(Tamburrino, Graziosi, and Bordegoni 2018; Obadimu and Kourousis 2021; Xiao et al. 2018). However, this method is known to be expensive and unreliable in the sense that part consistency is low and producing complex geometries with overhangs and supports are extremely difficult. Coupled with the defects occurring during production, namely voids, oxidation, and microstructural

inconsistencies (Echeta et al. 2020), the hybrid approach investigated in the second part of this work offers a substitute solution for producing polymer/metal composite lattice structures with desirable crashworthiness and impact energy absorbing performance that can be on par with their pure metal counterparts. Reviewing the literature, lattice structures produced by conventional metal AM methods such as selective laser melting (SLM), exhibit a broad spectrum of mechanical properties depending on the structure type, the material and relative density (Nazir et al. 2019; Riva, Ginestra, and Ceretti 2021; Hanks et al. 2020). To be able to consider the hybrid method a success the coated parts must achieve mechanical properties on par with their metal counter parts. For instance, (Yan et al. 2014) demonstrated that AlSi10Mg lattice structures produced by direct metal laser sintering (DMLS) exhibit compressive modulus in the range of 190 MPa with failure stresses up to 20 MPa. The collective available in the literature provide a better insight regarding the desirable performance that is expected from the composite parts studied in this part.

As the primary focus of this part is on the feasibility of the method, in-plane expanded hexagonal honeycomb is a good starting point due to simpler geometry that provides sufficient surface for coating (Habib et al. 2018a). More complex geometries can be studied in further investigations based on the result of this work. Composite materials employ the desirable properties of the involved components which in this part's case are NiCo alloy and rigid polyurethane polymer. The metal alloy provides much higher stiffness and mechanical properties while the core RPU segment allows for overall lighter weight structures.

1.5.4 Other applications of metallizing polymers.

Apart from the mechanical properties of metals, polymer/metal composites can benefit from other aspects of metal addition such as electrical and thermal conductivity, microwave compatibility, and so on. Selective electroless plating allows for embodying a connected network of conductive deposited wires that can function as circuits. Also, electroplating lightweight polymeric chambers allows the production of highly tunable and effective microwave guiding systems (Geterud, Bergmark, and Yang 2013; Ruskova et al. 2018; Park et al. 2017).

CHAPTER 2

PART 1.1: ELASTOMERIC PARTS PRODUCED BY DLS FOR MATERIAL CHARACTERIZATION

In this chapter we experimentally investigate the mechanical properties of parts printed from EPU 41 resin in accordance to the most conventional standards used in the literature. We fitted the experimental data with the most common models that accurately describe the hyperelastic and viscoelastic behavior of the EPU 41.

2.1 Experiment

The experimental samples were designed for mechanical property testing of standard test specimens or lattice materials. The material was EPU 41, an elastomer material available from Carbon 3D with a reported modulus of 6 MPa and strength of 6.2 MPa (Carbon3D Inc. 2018) (“The Promise of 3D Printing Fulfilled” n.d.). We fabricated a total of 27 specimens, designed for tensile, stress relaxation, and compression tests. Table 2.1 summarizes the specimen geometries and the measurement standards employed. Dimensions of all specimens were within $\pm 0.3\%$ of the respective designs, as verified by caliper measurements. Measurements were repeated on at least three identical specimens for each case and all measurements were made at standard room temperature.

Table 2.1 A summary of specimen types and tests employed.

Test	Specimen Geometry	Testing Standard	Number of Samples Tested
Tensile	Dog bone Type A and D (Figure 2.2)	ASTM D412 (D11 Committee n.d.)	6
Tensile stress relaxation	Dog bone Type A and D (Figure 2.2)	-	4
Compressive stress relaxation	Cylinder (Figure 2.6)	ASTM D6147 (D11 Committee n.d., 11)	3
Lattice compression	Lattice structures (Figure 3.1)	ASTM D1621 (D20 Committee n.d., 20)	8
DMA	Rectangular Slab	ASTM D4065 (D20 Committee n.d.)	3

The tensile tests and tensile stress relaxation tests used dog bone Type A and D geometries defined by ASTM D412 Standard Test Methods for Vulcanized Rubber and Thermoplastic Elastomers – Tension (D11 Committee n.d.). Testing was performed on a Zwick/Roell Z250 (Germany) universal testing machine (UTM). The type A tests used a 0.1 kN capacity load cell, and the type D tests used a 10 kN capacity load cell. The tensile tests were performed at a displacement rate of 500 mm/min. Figure 2.1 shows the specimen geometry of the ASTM D412 Type A

specimen, photographs of tensile and compressive printed specimens, and photographs of test setups.

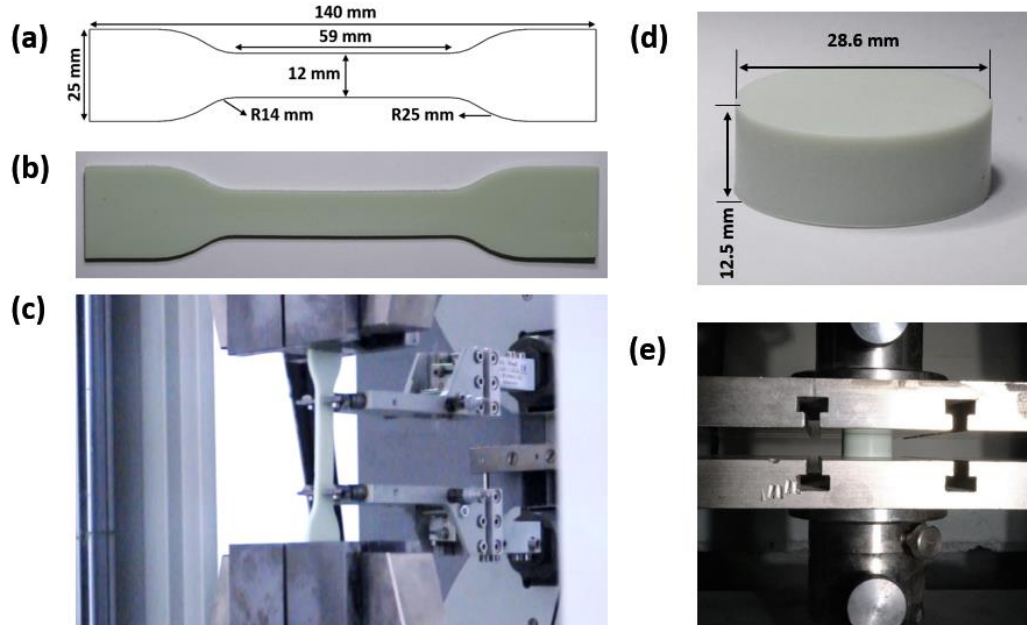


Figure 2.1 (a) Dimensions of the ASTM D412 specimen type A. (b) A photograph of a printed Type A specimen. (c) A photograph of the tensile testing setup. (d) Photograph of a printed cylindrical specimen with its dimensions. (e) Photograph of the compressive relaxation test setup.

For the tensile stress relaxation tests, we adopted standard procedures from the literature (Abayazid and Ghajari 2020; Adams et al. 2019) because there is no ASTM standard applicable for these tests. For tensile stress relaxation, the specimens were loaded to a target strain at a displacement rate of 500 mm/min and maintained constant displacement while monitoring the load for 2000 seconds. The machine repeated the measurements on the same specimen for five different target strains of 5%, 10%, 20%, 40%, and 60%. There was a 10-minute pause in the fully unloaded

state between each experiment to ensure complete recovery, verified by length measurements at the end of each pause.

The compressive stress relaxation measurements were made on cylindrical specimens with a diameter of 28.6 mm and a height of 12.8 mm according to the ASTM D6147 Standard Test Method for Vulcanized Rubber and Thermoplastic Elastomer – Determination of Force Decay (Stress Relaxation) in Compression (D11 Committee n.d.). Testing was performed on a Zwick/Roell Z020 (Germany) UTM combined with a 20kN rated load cell. The tests employed a constant strain target of 25%, corresponding to 3.125 mm of displacement. The displacement rate was 6.25 mm/min to ensure the strain target was reached within 30 seconds. Upon reaching the target strain, the load was measured over a period of 48 hours while maintaining a constant displacement.

The behavior of the elastomeric materials is known to be dependent on time, strain rate, and temperature (Abayazid and Ghajari 2020). In order to better understand how EPU 41 printed parts behave under different temperatures and loading rates we conducted dynamic mechanical analysis (DMA) tests on three 3D printed 2 mm x 5 mm x 20 mm parts in accordance with ASTM D4065 – 20 Standard Practice for Plastics: Dynamic Mechanical Properties: Determination and Report of Procedures (D20 Committee 2020). A Perkin Elmer Diamond DMA test module investigated the viscoelastic behavior of the samples both in temperature and frequency sweep modes under uniaxial tension loading. The temperature sweep test was set to cover a range of -100 C° to 100 C° with a load frequency of 1 Hz. For frequency sweep, we conducted the tests with varying frequencies ranging from 1 to 20 Hz.

2.2 Tensile Test Results

Figure 2.2(a) shows representative engineering stress-engineering strain data. The average stresses at 50% and 100% elongation are 2.5 and 4.4 MPa, respectively. The specimen ruptures at a tensile stress of 9.9 ± 1.3 MPa, corresponding to $173 \pm 9\%$ strain. Measurements on Type A and Type D specimens yielded nearly identical results (Type A not shown here). The tensile behavior is nonlinear throughout the elongation. The initial slope of the stress-strain curve up to 1% elongation is 10.6 MPa.

The measurement results are in good agreement with those reported in the material datasheet, which are based on measurements on Type C specimens at the same displacement rate of 500 mm/min. The primary difference is the considerably higher elongation at break in our measurements, which is about 40% larger than the value provided in the manufacturer datasheet. Also, the stress values for a given displacement are slightly lower in our case, but the difference remains within 10% for most of the data.

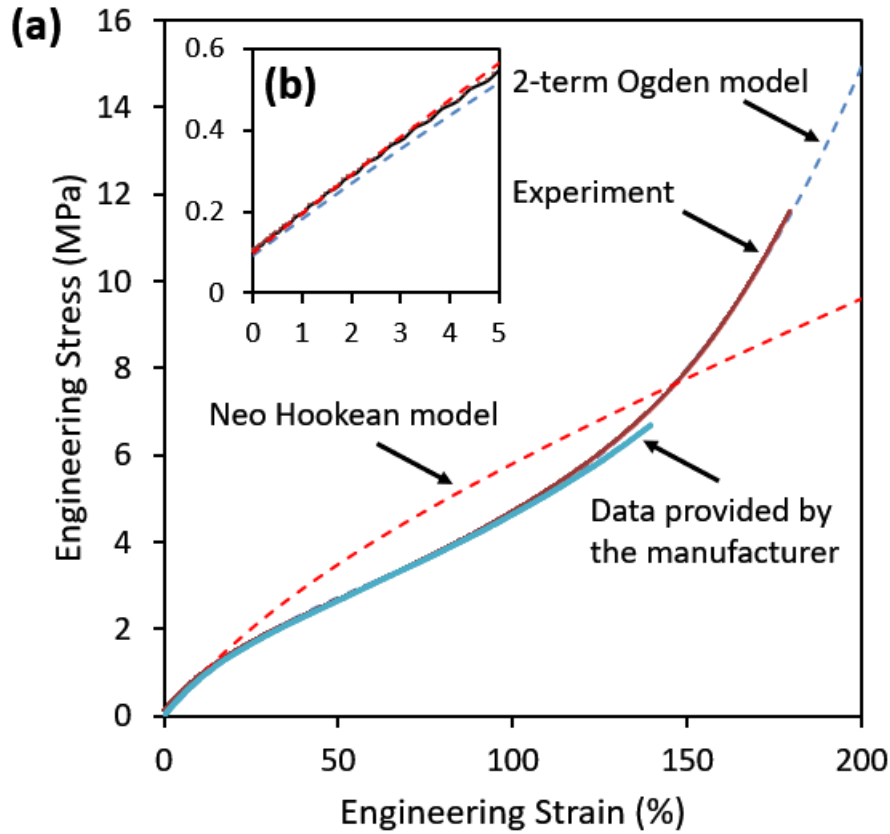


Figure 2.2. (a) Engineering stress vs. engineering strain behavior of EPU 41 under uniaxial tension. The data reported by the manufacturer is provided for comparison. The dashed lines show the predictions of Neo Hookean and Ogden models. (b) Data shown for small strains.

Next, we will fit the mechanical response of EPU 41 specimens under uniaxial tension using two different models, namely, the Neo Hookean hyperelastic model (Treloar 1943) and Ogden's model (Ogden and Hill 1972). The strain energy density function, W , of these models are defined as follows:

$$\text{Neo Hookean: } W = \frac{\mu_0}{2} (I_1 - 3) \quad (1)$$

$$\text{Ogden: } W(\lambda_1, \lambda_2, \lambda_3) = \sum_{p=1}^N \frac{2\mu_p}{\alpha_p^2} (\lambda_1^{\alpha_p} + \lambda_2^{\alpha_p} + \lambda_3^{\alpha_p} - 3) \quad (2)$$

where μ_0 is the initial shear modulus, I_1 is the first strain invariant, λ terms are the principal stretch ratios, and μ_p & α_p are material constants.

Figure 2.2(a) shows the predictions of the two hyperelastic models fitted using Hyperfit software with Nelder-Mead and Levenberg–Marquardt algorithms with fitting objective set on minimum square of the difference from the data (de Bortoli et al. 2011). The Neo Hookean model accurately models the stress-strain behavior of EPU 41 up to a strain of about 15%, and has lower accuracy at higher strains, which is commonly observed for many other elastomers (Treloar 1943). The Ogden model accurately models the experimental data accurately until rupture with R^2 values above 0.99. Figure 2.2(b) shows a the model for small strains, demonstrating that the Neo Hookean model is slightly more accurate in this range.

2.2.1 Modeling of the Hyperelastic Response

One can describe the hyperelastic response of an isotropic elastomer by employing the strain energy density function:

$$W = W(I_1, I_2, I_3) \text{ or } W = W(\lambda_1, \lambda_2, \lambda_3) \quad (3)$$

Where I terms are the strain invariants of the Cauchy-Green Tensor and λ terms are the principal stretch ratios. Then the corresponding deformation gradient tensor \mathbf{F} in terms of principal stretches becomes:

$$\mathbf{F} = \begin{bmatrix} \lambda_1 & 0 & 0 \\ 0 & \lambda_2 & 0 \\ 0 & 0 & \lambda_3 \end{bmatrix} \quad (4)$$

Accordingly, the Jacobian determinant of the deformation tensor is as follows.

$$J = \det(\mathbf{F}) = \lambda_1 \lambda_2 \lambda_3 \quad (5)$$

For this deformation state, strain invariants are calculated as follows:

$$I_1 = \lambda_1^2 + \lambda_2^2 + \lambda_3^2 \quad (6)$$

$$I_2 = \lambda_1^2 \cdot \lambda_2^2 + \lambda_2^2 \cdot \lambda_3^2 + \lambda_1^2 \cdot \lambda_3^2 \quad (7)$$

$$I_3 = \lambda_1^2 \lambda_2^2 \lambda_3^2 \quad (8)$$

Based on bulk modulus measurements, EPU 41 can be assumed as incompressible, similar to most other elastomers, resulting in a Poisson's ratio of 0.5. As a result, λ_1 fully defines the strain state of an incompressible isotropic hyperelastic material under uniaxial loading, and λ_2 and λ_3 become functions of λ_1 , as follows.

$$\lambda_1 = \lambda = \frac{l}{l_0}, \quad \lambda_2 = \lambda_3 = \frac{1}{\sqrt{\lambda}} \quad (9)$$

Lastly, the stress state of a hyperelastic elastomer under simple uniaxial tension can be written as (Holzapfel 2002):

$$\sigma_{11} = 2 \times \left(\lambda^2 - \frac{1}{\lambda^2} \right) \left[\frac{\partial W}{\partial I_1} - \frac{1}{\lambda} \frac{\partial W}{\partial I_2} \right] \quad (10)$$

The first strain energy density model that we consider is the Neo Hookean hyperelastic model, which is a single-parameter constitutive function in terms of the first strain invariant I_1 (see Eq.(6)) (Treloar 1943):

$$W = \frac{\mu_0}{2} (I_1 - 3) \quad (11)$$

where μ_0 is the initial shear modulus of the material. While Neo Hookean model is only accurate for small strains, it is one of the most commonly used models as a first approximation due to its simplicity and foundations on the statistical thermodynamics of polymer chains.

Among numerous models developed to describe the nonlinear hyperelastic behavior of elastomeric materials more accurately (Dal et al. 2019), we will employ Ogden's model (Ogden and Hill 1972) as a second approach. This model can accurately capture the nonlinear stress-strain behavior for elongations exceeding 700% (Dal et al. 2019). The model utilizes a phenomenological function of principal stretches as follows.

$$W(\lambda_1, \lambda_2, \lambda_3) = \sum_{p=1}^N \frac{2\mu_p}{\alpha_p^2} (\lambda_1^{\alpha_p} + \lambda_2^{\alpha_p} + \lambda_3^{\alpha_p} - 3) \quad (12)$$

Substituting this expression into Eq. (10) we can determine the uniaxial stress-strain response as follows.

$$\sigma_{11} = \sum_{p=1}^N \frac{2\mu_p}{\alpha_p} \left(\lambda^{\alpha_p-1} - \lambda^{-\left(\frac{\alpha_p}{2}+1\right)} \right) \quad (13)$$

In this equation, μ_p and α_p are material constants, and N is the number of terms used in the constitutive equation. The sum of the μ_p terms provides the initial shear modulus of the incompressible hyperelastic material, μ_0 .

Figure 2. (d) provides the predictions of these two hyperelastic models fitted using Hyperfit with Nelder-Mead and Levenberg–Marquardt algorithms (de Bortoli et al. 2011). Table 2.2 summarizes the fitting constants. The results show that the Neo Hookean model is capable of accurately describing the stress-strain behavior of EPU 41 up to a strain of about 15% and starts losing its accuracy rapidly at higher strains, a common behavior of the model also observed for many other elastomers (Treloar 1943). On the other hand, the Ogden model captures the experimental data accurately until rupture with R^2 values above 0.99. Figure 2. (e) shows a closer look at the model

predictions for small strains, demonstrating that the Neo Hookean model is slightly more accurate in this range. Figure 2.3 shows the tensile test results and corresponding fitting curves for a Type A specimen compared to the data provided from manufacturer.

Table 2.2. Constants of the curve fit for 2-term Ogden and Neo Hookean hyperelastic models.

2-term Ogden			Neo Hookean	
μ_1	α_1	μ_2	α_2	μ_0
0.173	5.823	2.957	-0.266	3.327

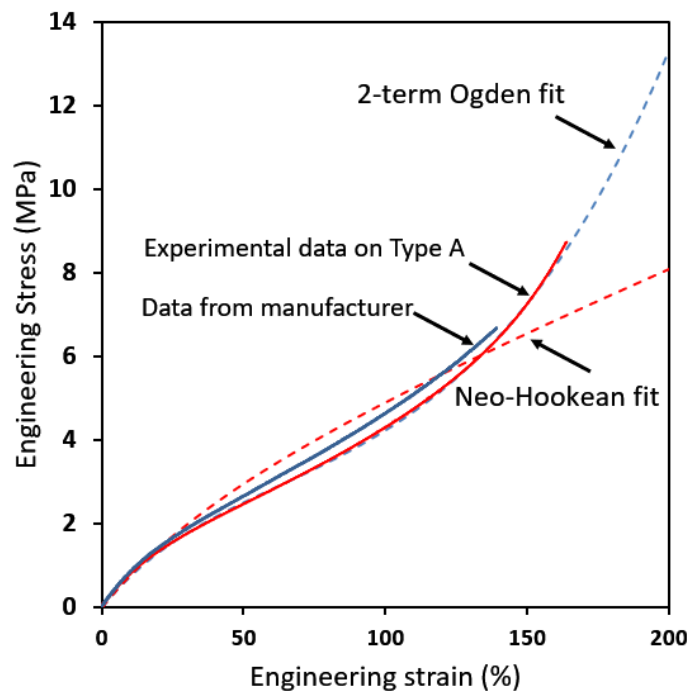


Figure 2.3. Stress vs. Strain data for EPU 41 from tensile experiment on a Type A specimen, fitting curve obtained from 2-term Ogden and Neo-Hookean Models, and the data provided from the manufacturer.

2.3 Stress Relaxation Test Results

Figure 2.4 shows the tensile stress relaxation behavior measured at five different strains. Figure 3(a) shows the measured stress as a function of time. The initial stress-strain responses are nearly identical for the series of loadings performed sequentially on the same specimen. Upon reaching the target strain, the stress relaxation starts and proceeds with a gradually decreasing rate.

Figure 2.4(b) shows the relaxation modulus as a function of time, where E is defined as

$$E(t) = \frac{\sigma(t)}{\varepsilon_0} \quad (14)$$

The relaxation modulus first decreases rapidly and then reaches a plateau. The plateau modulus depends on the initial strain; it decreases from 7.2 MPa to 3.7 MPa as the initial strain increases from 5% to 60%. The inset of Figure 2.4(b) shows the relaxation modulus normalized by the peak stress, σ_0 . The normalized stress decays similarly for each case. The initial segment of about 20 seconds shows a relatively rapid drop in stress, and then the relaxation rate gradually decreases. The normalized relaxation reaches about 28% by 2000 s. Overall, the results exhibit typical trends of stress relaxation, where the rate of the decrease in stress monotonically decreases. The overlap of the initial loading segments shows that the 10-minute pauses between each loading have been long enough to ensure complete recovery, suggesting that Mullin's effect is virtually absent (Diani, Fayolle, and Gilormini 2009).

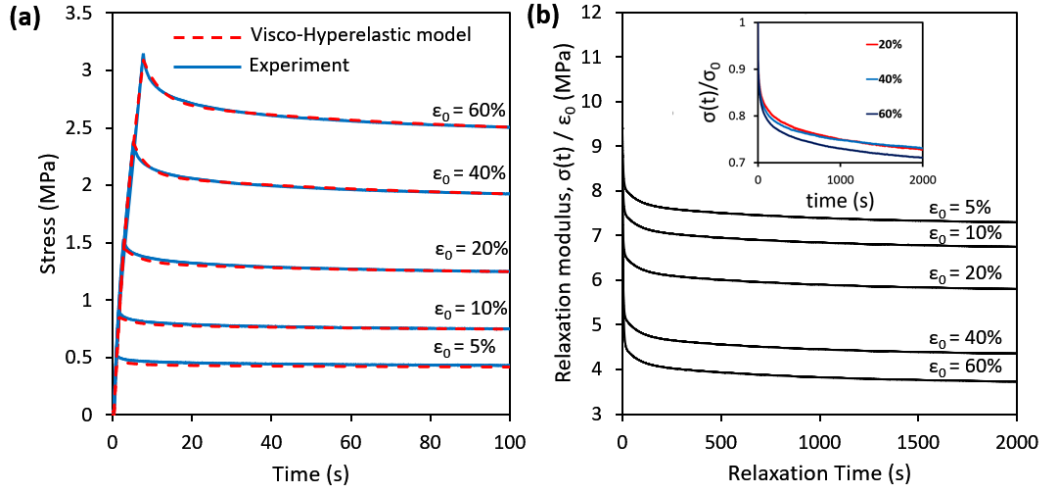


Figure 2.4. (a) Stress relaxation behavior of EPU 41 after rapid tensile loading. Dashed lines show the predictions of the visco-hyperelastic model. (b) Relaxation modulus variation for the whole duration of the experiment. Inset shows the normalized stress, σ / σ_0 , vs. time.

Another interesting observation is the dependence of the plateau relaxation modulus on the strain applied. This dependence is an outcome of the nonlinear response of the elastomers, also observed for EPU 40 (Hossain, Navaratne, and Perić 2020). Specifically, the monotonically decreasing elastic modulus with increasing strain up to about 62% strain can explain this trend, as modulus is directly proportional to the relaxation rate and the S-shaped response of elastomer materials remains the same in the relaxed state (Davidson and Goulbourne 2013).

We model the stress relaxation behavior by combining time-dependent and time-independent stress contributors (Abayazid and Ghajari 2020; Kraus et al. 2017). The model employs a three-term Prony series based on the generalized Maxwell model, where each term corresponds to a Maxwell-Weichert spring-dashpot pair represented in Figure 2.5, as follows.

$$E(t) = E_{\infty} + \sum_{i=1}^3 k_i e^{-\frac{t}{\tau_i}} \quad (15)$$

$$\sigma(t) = \sigma^{ins} - \varepsilon_0 \times \sum_{i=1}^3 k_i \left(1 - e^{-\frac{t}{\tau_i}}\right) \quad (16)$$

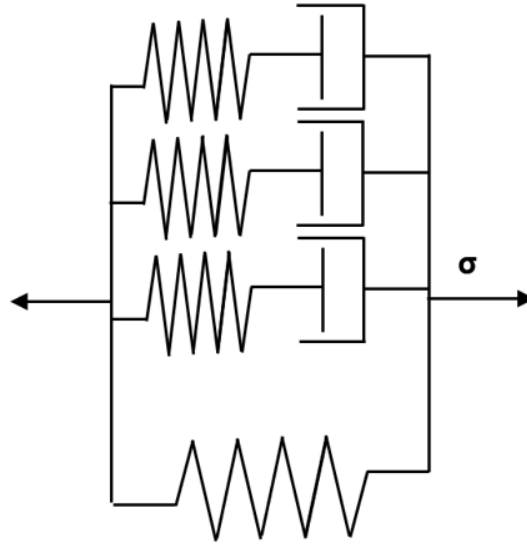


Figure 2.5. Representation of Generalized Maxwell model, employing a series of spring-dashpot elements for viscosity and time dependent behavior of materials (A. Alperen Bakır, Neshani, and Özerinç 2021)

In this equation, σ^{ins} is the time-independent instantaneous stress term based on the Ogden hyperelastic model we utilized for predicting the uniaxial tensile behavior. k_i and τ_i are the relaxation moduli and relaxation times, respectively. MATLAB's cftool toolbox calculated the constants of Eq.(16), which are provided in Table S2. The model results are shown in Fig 3(a), demonstrating excellent agreement with the experimental results. The Prony series assumes linear viscoelasticity, which ignores the nonlinear response of EPU 41 at large deformations. Nevertheless, the

predictions are satisfactory, which is consistent with observations made for other nonlinear elastomers (Robinson et al. 2019; Pelayo et al. 2021; Reppel and Weinberg 2018).

Table 2.3. Prony series constants obtained after fitting the model to experimental results.

	K_1	K_2	K_3	τ_1	τ_2	τ_3		
Tensile Stress Relaxation	0.78	0.51	0.69	4.9	79	863		
	K_1	K_2	K_3	K_4	τ_1	τ_2	τ_3	τ_4
Compressive Stress Relaxation	1.511	1.448	1.187	1.43	6.5	129	3561	7.0×10^4

Figure 2.6 shows the compressive stress relaxation experiments. Figure 2.6(c) shows the relaxation of stress as a function of time, with the insets showing load vs. displacement and load vs. time behavior. The stress decreases from 3.4 MPa to 2.0 MPa after 48 hours, corresponding to a relaxation of 40%. 65% of this relaxation occurs within the first 30 minutes. The 48-hour constant-strain loading resulted in a compressive set of 13%, and the puck restored its initial dimensions in about an hour. A four-term Prony series approximated the experimental compressive relaxation test data by considering the reference time as the onset of reaching the constant 25% strain.

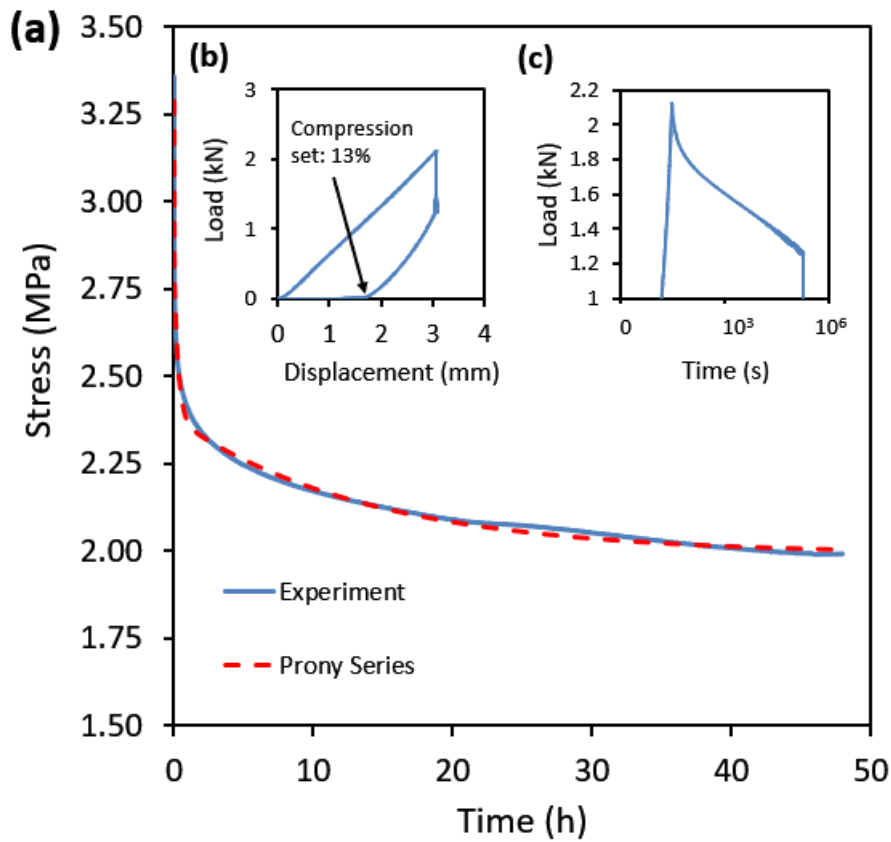


Figure 2.6. (a) 48-hour stress relaxation response under compression. The dashed line indicates the Prony series fit. (b) The corresponding load vs. displacement data, showing 13% compression set upon unloading. (c) The corresponding load vs. time data.

2.4 Further discussion on the hyperelastic and viscoelastic models

Phenomenological hyperelastic models consider the principal stretches that occur during deformation. Given that Ogden model incorporates all three principal stretches in order to achieve robust and correct material constants, equiaxial or biaxial test data are also required in the sense that Ogden model when is fitted only to uniaxial test results tend to overestimate the loading response in the other two

principal directions, reportedly up to 300%. Several different hyperelastic models have been proposed with different approaches regarding the modeling of elastomers namely, extended networks of chains, i.e. 8-chain model, or spherical elements. Arruda-Boyce hyperelastic model (Arruda and Boyce 1993; Boyce and Arruda 2000) is one such method that performs better than Ogden. Recently, Extended 8-chain model (Dal, Gültekin, and Açıkgöz 2020) has been proposed by incorporating the second strain tensor invariant that alleviates the overestimation problem. The author encourages the readers to use the provided references that provide exceptional and in-depth study on the performance of various hyperelastic models (Dal et al. 2019; Dal, Açıkgöz, and Badienia 2021).

The time and strain rate dependent behavior of elastomers that exhibit in the form of viscoelasticity is nonlinear by nature. While the hyper-viscoelastic formulation used in this work captures the relaxation behavior of EPU 41 accurately, however, the basis of the models is linear. In the light of the newly proposed extended 8-chain model, by employing nonlinear Maxwell-Weichert elements a much accurate model is available that has been successfully demonstrated its remarkable performance by fitting experimental data for both creep compliance and stress relaxation tests even for large strains. For in depth detail of this approach the author encourages the readers to refer to this state-of-the-art model that has been introduced (Dal, Gültekin, and Açıkgöz 2020).

2.5 Dynamic Mechanical Analysis Results

The behavior of the elastomeric materials is known to be dependent on time, strain rate, and temperature (Abayazid and Ghajari 2020). In order to better understand how EPU 41 printed parts behave under different temperatures and loading rates we conducted dynamic mechanical analysis (DMA) tests on printed 2 mm x 5 mm x 20 mm parts in accordance with ASTM D4065 – 20 Standard Practice for Plastics: Dynamic Mechanical Properties: Determination and Report of Procedures (D20 Committee 2020). A Perkin Elmer Diamond DMA test module investigated the viscoelastic behavior of the samples both in temperature and frequency sweep modes under uniaxial tension loading. The temperature sweep test was set to cover a range of -100 C° to 100 C° with a load frequency of 1 Hz. For frequency sweep, we conducted the tests with varying frequencies ranging from 1 to 20 Hz. Figure 2.7 shows the results of the 1 Hz temperature sweep and compares the results to the data provided by the vendor. The measured Storage and Loss Moduli, E' and E'' refer to the amount of energy stored inside of the sample during the loading phase and subsequently, the amount of energy that has been lost thermodynamically when the sample undergoes the unloading phase while redirecting the stored energy. Moreover, the magnitude of displacement and force in the sample follows the loading cycle with a phase shift (lag) that can be assessed using a parameter called loss factor or $\tan \delta$ (TanD) which is the tangent of the shifted phase angle. It is calculated by dividing the loss modulus by storage modulus. When plotted versus temperature, the peak point of the loss factor curve indicates a critical temperature

called glass transition temperature T_g . below this temperature, a rubbery material will lose its elastic properties and behave like brittle glass. Another significance of the loss factor graph is the indication of the elastic region, a plateau within a range of temperature where the material can retain its elastic behavior. Beyond the endpoint of the plateau region, the material either starts to flow in a fluid-like manner or starts to degrade(International Seminar: Thermal Analysis and Rheology, Ramon, and Inc 2005). The test result shows that EPU 41 has a T_g of nearly -11 C° (lower than the claimed -9 degrees in the datasheet) and can retain its elastic modulus up to 100 C° .

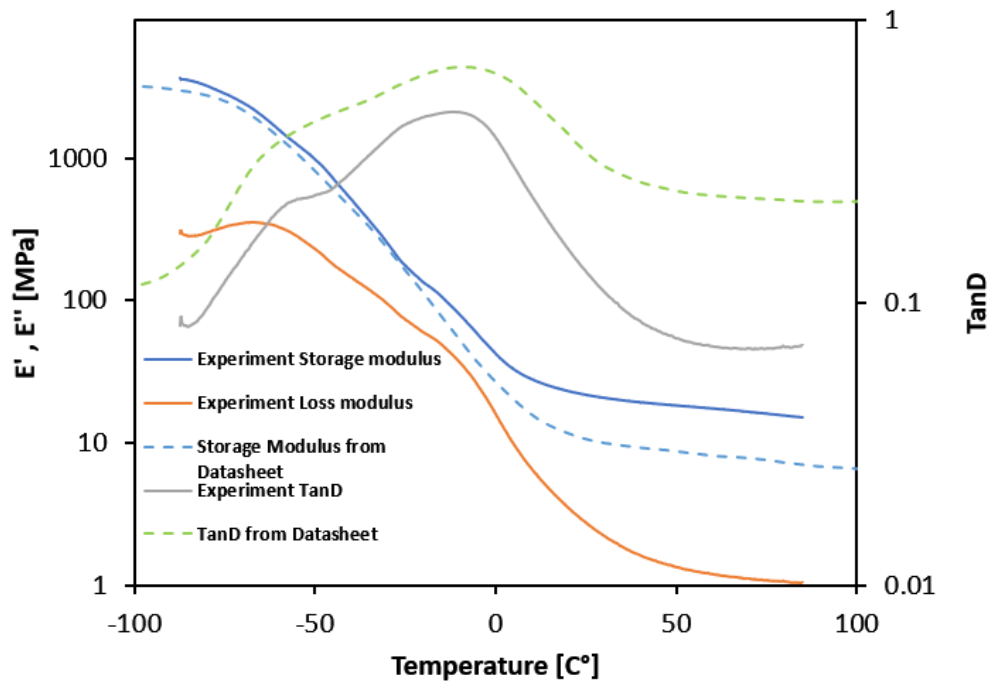


Figure 2.7. temperature sweep test result from DMA test compared to the data provided by the vendor for EPU 41.

Figure 2.8(a) shows the results of the frequency sweep test. Figure 2.8(b) summarizes the test results for T_g showing that increasing the strain rate results in

higher glass transition temperatures as expected. By increasing load frequency from 1 Hz to 20 Hz the T_g increase by 12 degrees.

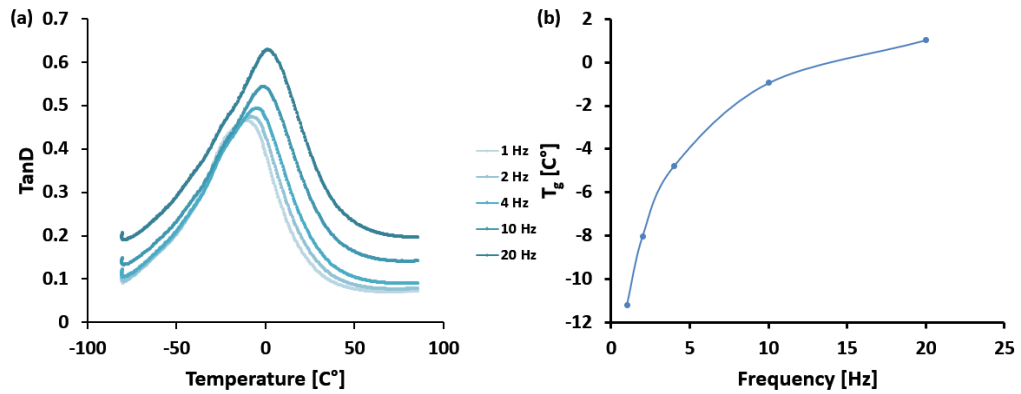


Figure 2.8. (a) Frequency sweep test results from multiple DMA tests. (b) glass transition temperature's shift trend with relation to loading frequency.

CHAPTER 3

PART 1.2: ELASTOMERIC LATTICE STRUCTURE PARTS PRODUCED BY DLS

In this part chapter we examined the energy absorption properties of three different types of lattice structures and compared their effectiveness in regards to their quasi-static compressive behavior.

3.1 Design and Preparation of the Lattice Parts

The lattice compression measurements tested specimens of three different lattice architectures: either cubic, octet-truss (will be referred to as octet), and body-centered cubic + cubic primitive (BCC+CP) with different strut diameters. These cubic prism based structures are among the most common geometries studied in the field of lattice architectures (Nazir et al. 2019). The unit cells are designed based on geometric wireframe and then by employing direct patterning the overall structure takes form (Beyer and Figueroa 2016; Helou and Kara 2018; Pan, Han, and Lu 2020). The struts had circular cross-sections, apart from the bottom surface exhibiting a flat base. Cubic and BCC+CP specimens consisted of $4 \times 4 \times 4$ cells, and the Octet specimens consisted of $3 \times 3 \times 3$ cells with $30 \times 30 \times 30$ mm overall dimensions for all specimens. Figure 3.1 shows solid models of the unit geometry, photographs of specimens, and the test setup for each case.

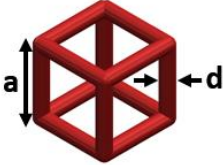
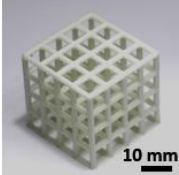
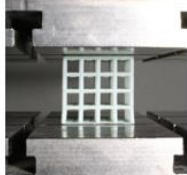

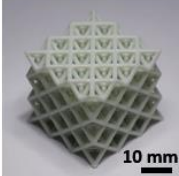

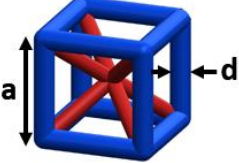
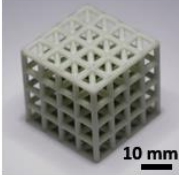
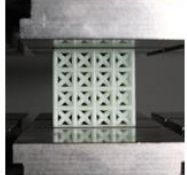
Cell Type	Unit Cell Model	Printed Specimen	Test Setup
Cubic			
Octet Truss			
BCC + CP			

Figure 3.1. The solid models of each unit cell type, photographs of printed specimens, and photographs of the test setup. The truss length is a , and the truss diameter is d .

Table 3.1 summarizes the dimensions of the lattice parts and shows the specimen names. Relative density (ρ^*) corresponds to the solid volume fraction and can be written as (I. J. Gibson and Ashby 1982):

$$\rho^* = \frac{\rho_{\text{lattice}}}{\rho_{\text{solid}}} \quad (17)$$

where ρ_{lattice} is the apparent density of the lattice structure, obtained by dividing the measured mass by the measured volume occupied by the boundaries of the lattice. ρ_{solid} is the density of 100% filled EPU 41. Our measurements on solid cylindrical specimens printed for compressive stress relaxation provided a density of 1.028 g/cm³, in agreement with the manufacturer data sheet.

Another critical parameter for lattice structures is the slenderness ratio of the struts, defined as the effective length of the struts divided by its gyration radius, K (Alghamdi et al. 2021):

$$SR = \frac{a}{K} \quad (18)$$

K is defined as the ratio of the second moment of area, I , to the cross-sectional area of the strut, as follows:

$$K = \sqrt{\frac{I}{A}} = \sqrt{\frac{\frac{\pi}{64} d^4}{\frac{\pi}{4} d^2}} = \frac{d}{4} \quad (19)$$

where d is the strut diameter.

Table 3.1 Summary of the lattice parts produced and some key parameters.

Type	Number of cells	Specimen Name	Truss diameter, d (mm)	Truss length, a (mm)	Relative Density (%)	Slenderness Ratio
BCC+	4 × 4 × 4	BCC+CP 1	1.0	8.5	12.9	34
CP		BCC+CP 2	2.0	9.5	40.3	19
Cubic	4 × 4 × 4	Cubic 1.5	1.5	8.5	11.5	23
		Cubic 2	2.0	9.5	19.3	19
Octet truss	3 × 3 × 3	Octet 1	1.0	16.0	11.8	32
		Octet 1.5	1.5	17.0	26.1	23
		Octet 2	2.0	18.0	40.8	18

Compression tests on lattice specimens followed the ASTM D1621 Standard Test Method for Compressive Properties of Rigid Cellular Plastics (D20 Committee n.d.). Tests were performed on a Zwick/Roell Z020 UTM with a unit cell rated for 20 kN. The displacement rate was 10% of specimen height per minute (0.00167 s^{-1} strain rate), ensuring quasi-static loading. The compression tests employed four loadings and unloading cycles, with strain limits of 5%, 13%, 50%, and 75%. There was a 10-minute pause in the fully unloaded state in between each experiment to ensure complete recovery. A Fujifilm X-S10 Mirrorless Camera equipped with an XF16-80mm F4 R OIS WR objective lens recorded the compression tests at 240 frames per second.

3.2 Lattice Compression Test Results

Figure 3.2 shows the results for the Cubic 2 lattice structure under compression. Figure 3.2(a) displays the force and displacement behavior for the four cases of target strains. The main figure shows the first three cases, and the inset shows the 75% strain target case. The loading curves with different strain targets are nearly the same. The force-displacement curves exhibit a linear and sharp rise up to 0.05 strain, followed by a plateau region. After reaching a strain of 0.68, the slope increases as the part densifies until the end of compression, $\varepsilon = 0.75$.

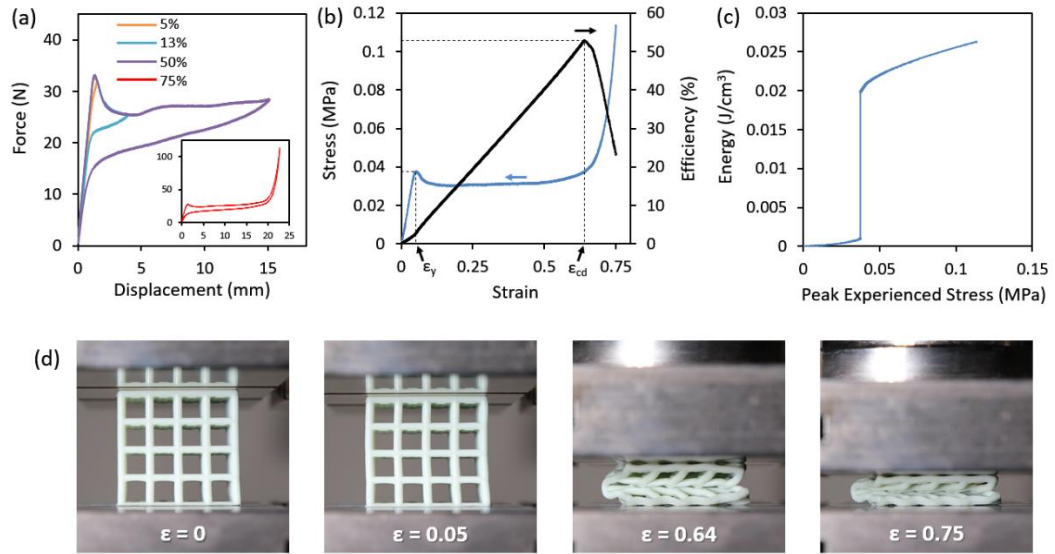


Figure 3.2. (a) Force vs. displacement response of a Cubic 2 sample for four different strain targets. (b) Stress-strain behavior and the efficiency of the lattice as a function of strain. (c) Corresponding energy diagram of the lattice under compression. (d) Snapshots from the test footage at different strains.

The force-displacement behavior of the Cubic 2 is analogous to those exhibited by foams; an initial linear response until buckling, followed by a plateau region, and eventual rapid rise in stress. The point of buckling marks the yield stress, ϵ_y , of the structure, determined by either the peak stress or a disturbance in the efficiency curve when a peak is not available, as explained in further detail below. The plateau corresponds to the gradual collapse of struts on each other. During this process, the load required for further deformation is mediated by the deformation of the cells in the process of collapsing, resulting in approximately constant values of stress. The next stage is a rapid rise in the stress upon the completion of the collapse called the critical densification strain (ϵ_{CD}), determined by the location of the shoulder in the efficiency curve (see Figure 3.2(b) and the following discussion). Any further strain is predominantly realized by the elastic deformation of the solid (Nayak and Tripathy

2002). At this stage, there is usually still some more room for densification due to the rising load, which results in the observed monotonous increase in the load-displacement slope.

The next step is the structure's efficiency and energy storage analysis, which provides insight into the impact absorbance performance. The first parameter to consider is the amount of absorbed energy, W , which corresponds to the area underneath the stress-strain curve.

$$W = \int_0^{\varepsilon} \sigma(\varepsilon) d\varepsilon \quad (20)$$

where σ and ε are the stress and strain, respectively, calculated by using the overall dimensions of the lattice part. Based on the absorbed energy behavior, one can define efficiency as a function of strain, which compares the performance of the lattice structure to that of an ideal foam having a density close to zero, as follows (Habib et al. 2018b).

$$E(\varepsilon) = \frac{\int_0^{\varepsilon} \sigma(\varepsilon) d\varepsilon}{\sigma_p(\varepsilon) \times 1} \times 100 \quad (21)$$

Where σ_{ideal} in the denominator of Eq.(21) is replaced by the peak stress, $\sigma_p(\varepsilon)$, the highest stress measured up to the strain under consideration for the lattice part.

Figure 3.2(b) and (c) presents the results of the analysis. Figure 3.2(b) shows the variation of efficiency with strain, together with the stress-strain response. The efficiency increases linearly and reaches a peak value of 51.7%, beyond which a monotonic decrease starts. This peak value marks the point of critical densification strain, which corresponds to the completion of the collapse of the layers of struts.

Beyond this point, the compression is mediated by the deformation of the solid part, which is the cause of the rapid rise in force (see Figure 3.2(a)). The very beginning of the efficiency curve exhibits a nonlinear segment, and the transition from this regime to the linear one marks the yield point of the lattice structure, which also corresponds to the onset of buckling.

Next, Figure 3.2(c) shows the so-called energy diagram of the structure, directly calculated from Eq. (20). The x-axis is the peak experienced stress, defined as the maximum stress encountered up to the corresponding strain of the energy data. The energy diagram of Cubic 2 exhibits a shoulder with a virtually constant peak stress segment, a common feature observed in the majority of energy-absorbing structures (Maiti, Gibson, and Ashby 1984). Starting with the vertical part of the curve, the structure starts to absorb a considerable amount of energy without any significant rise in the experienced stress. A more pronounced vertical segment indicates a higher energy absorbance performance for the respective lattice structure.

Table 3.2 summarizes the key parameters such as yield stress, densification strain, plateau stress, and efficiency for Cubic 2 and all other lattice geometries considered in this study. The elastic modulus values reported in the table were calculated over the linear portion of the respective stress-strain responses (Bagheri et al. 2018).

Figure 3.3 and Figure 3.4 show the same data for the Octet 1 and BCC+CP 2 structures. While the main features of the load-displacement data are similar to that of the cubic, there are several differences.

The Cubic 2 structure exhibits a rapid softening right after the peak load due to the buckling of the structure as a whole. On the other hand, the Octet 2 structure exhibits almost no softening due to the stretching-dominated deformation in these structures.

Cubic 2 has a relatively smooth and virtually constant load response in the plateau. The octet structure, on the other hand, exhibits load oscillations and an upward trend. The oscillations are due to the nodal rearrangements that modulate the instantaneous stiffness of the geometry (Ling et al. 2019).

The efficiency and energy curves of Octet 1 and BCC+CP 2 also differ. Octet 1 exhibits oscillations in the rising segment of the efficiency, whereas BCC+CP 2 has a more curved hump with a narrow linear zone.

At this point, Maxwell stability criterion helps to make a distinction between different types of lattice structures. The criterion separates lattice structures into two classes depending on the dominating deformation behavior through the Maxwell number, M , defined as follows.

$$M = b - 3j + 6 \tag{22}$$

where b is the number of struts and j is the number of nodes inside the unit cell. Lattice structures with a negative Maxwell number are under-stiff and bending dominated, while structures with zero or positive numbers are over-stiff and stretching dominated (Austermann et al. 2019; Ashby 2006). In this work, the Maxwell number for Cubic, Octet, and BCC+CP lattice structures are -6, -1, and 0, respectively. According to this categorization, Cubic and Octet lattices are bending-

dominated, whereas BCC+CP is stretch-dominated, which explains the distinction between the observed responses.

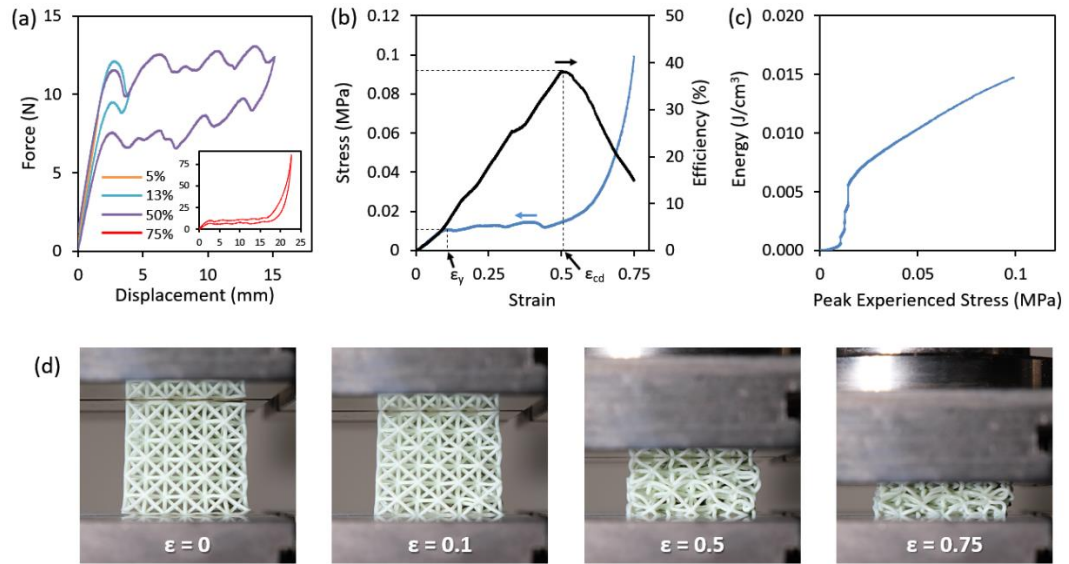


Figure 3.3 (a) Force vs. displacement response of an Octet 1 sample for four different strain targets. (b) Stress-strain behavior and the efficiency of the lattice as a function of strain. (c) Corresponding energy diagram of the lattice under compression. (d) Snapshots from the test footage at different strains.

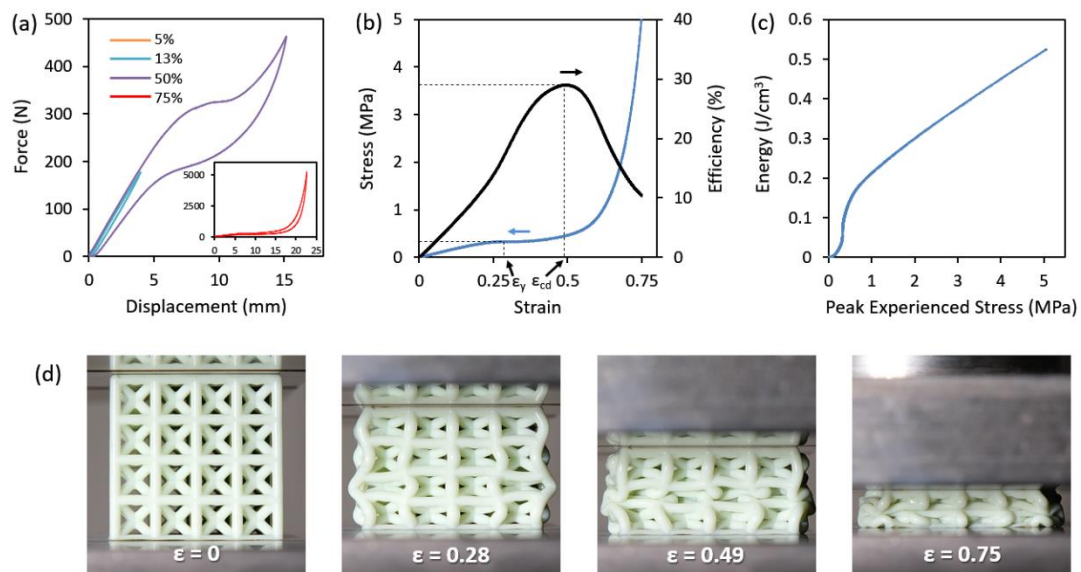


Figure 3.4 (a) Force vs. displacement response of a BCC + CP 2 sample for four different strain targets. (b) Stress-strain behavior and the efficiency of the lattice as a function of strain. (c) Corresponding energy diagram of the lattice under compression. (d) Snapshots from the test footage at different strains.

Table 3.2. Summary of the quasi-static compression test results for different lattice structures.

Sample Name	Maximum Efficiency (%)	Relative density (%)	Densification Strain (porosity)	Critical Densification Strain	Plateau Stress (MPa)	Yield Stress (MPa)	Elastic Modulus (MPa)
BCC+CP 2	28.9	40.3	0.59	0.49	0.340	0.328	1.49
BCC+CP 1	42.1	12.9	0.87	0.52	0.018	0.014	0.25
Cubic 2	52.9	19.3	0.81	0.64	0.032	0.037	0.87
Cubic 1.5	47.5	11.5	0.88	0.64	0.009	0.007	0.30
Octet 1	38.3	11.8	0.88	0.50	0.012	0.011	0.13
Octet 1.5	39.3	26.1	0.74	0.51	0.075	0.075	0.43
Octet 2	34.3	40.8	0.59	0.51	0.230	0.212	0.96

The comparison of the results for each case demonstrates the effect of lattice geometry on the mechanical response. In addition, strut diameters and the respective slenderness ratios can drastically change the deformation behavior and energy capacity.

3.3 Effect of Slenderness Ratio on the Performance Metrics

Figure 3.5 shows the effect of lattice geometry and the slenderness ratio on a wide range of performance metrics.

First of all, Figure 3.5(a) shows the relative density with respect to the slenderness ratio. While the decrease in the density with slenderness ratio comes from the definitions of each term, the cubic structure's lower relative density highlights the major difference between the cubic and the other structures, which are also reflected in the mechanical response for most cases as discussed next.

Figure 3.5(b) shows the critical densification strain (CDS). CDS remains around 0.5 for BCC+CP and Octet geometries, whereas the cubic structure has a higher value of 0.64. An examination of Figure 3.5(a) and Figure 3.5(b) shows no direct correlation between the relative density and the CDS values. While the relative densities exhibit a wide range of values (10% - 40%), the CDS values are confined to a narrow range of 0.5 – 0.65. In theory, the densification strain marked by the end of the plateau is equivalent to the porosity, that is, $1 - \rho^*$. However, in reality, densification begins at lower strain levels as the struts cannot collapse on each other perfectly, leaving some gaps, especially in the vicinity of the nodes, which explains the observed behavior.

The slenderness ratio does not strongly influence CDS either, as observed previously (Ling et al. 2019). We explain this behavior by the cell sizes that are very close to each other. The unit cell size directly influences the length scales of the buckling and collapsing behavior, which in turn determines the collapsing efficiency to a great extent.

Figure 3.5(c) shows the elastic modulus data. As the slenderness ratio increases, the modulus values decrease. This is an expected trend as modulus values based on the

initial stage of loading are strongly correlated with the load-bearing cross-section. The BCC+CP 2 samples exhibit the highest stiffness, which in fact, has the largest solid area fraction among the samples.

Figure 3.5(d) shows the yield strain values of the structures. The yield strain monotonically decreases with the slenderness ratio for any give lattice geometry. While BCC+CP and Octet structures exhibit almost the same trend with slenderness ratio, Cubic structures' yield strain is considerably lower. This is due to the buckling-dominated deformation behavior, which causes large deformations at relatively lower loads. When it comes to the corresponding yield stresses (Figure 3.5(d)), the trends are analogous. The major difference is the higher yield stress of the BCC+CP compared to the Octet structure.

Figure 3.5(f) shows the plateau stresses, which exhibit almost the same behavior as the yield stress. Cubic structures have an exception here; there exist obvious peaks in stress and subsequent softening in the plateau regime caused by the severe buckling.

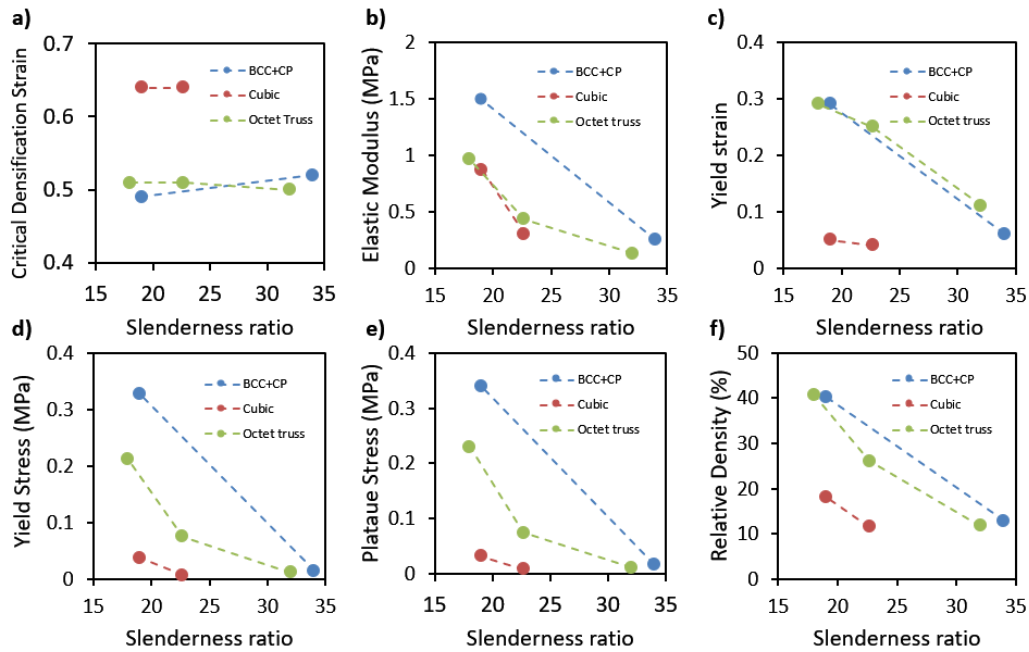


Figure 3.5. Effect of slenderness ratio on a wide range of compressive performance metrics for Cubic, BCC+CP, and Octet lattice structures.

3.4 Comparison of the performance of all the lattice structure types

Lastly, we compare the absorbed energy and stress-strain behavior of all samples in Figure 3.6. As the lattice parts exhibited large differences in energy absorbance capacities and stress values, the figure shows the results in a density-normalized format.

Figure 3.6(a) shows the energy absorbed per unit mass (J/g) as a function of the peak specific stress for each sample under quasi-static compression. This plot provides an indication of the energy absorbance capacity at the corresponding stress; for example, Cubic 1 sample has 0.1 J/g maximum energy capacity, implying that a Cubic 1 lattice structure with 1 kg mass would absorb 100 J while transferring a specific peak stress of 0.05 MPa/(kg/m³).

A comparison between different samples should consider both the absorbing capacity and the amount of transferred stress. As discussed previously, a more pronounced vertical segment in an energy diagram indicates higher capacity. According to this criterion, Octet 2 exhibits superior performance compared to the BCC+CP with similar density, in agreement with the literature (Nazir et al. 2019). On the other hand, among the samples with lower densities around 10%, namely, Cubic 1.5, Octet 1, and BCC+CP 1, BCC+CP 1 shows the best performance.

Figure 3.6(b) shows the specific stress vs. strain of all lattice structures. Cubic samples have the most extended plateau region, with an energy absorption range reaching nearly 60% strain. On the other hand, the plateau region is the shortest for BCC+CP 2, demonstrating that it does not provide an ideal solution to energy-absorbing applications. Note that an entirely fair and universal comparison between the samples is not possible in the context of these figures, as the compromise between the peak stress and energy absorption capacities are often application dependent. When the application requirements set the acceptable ranges of stress and energy, then such diagrams can be used effectively to select among the alternative geometries and slenderness ratios.

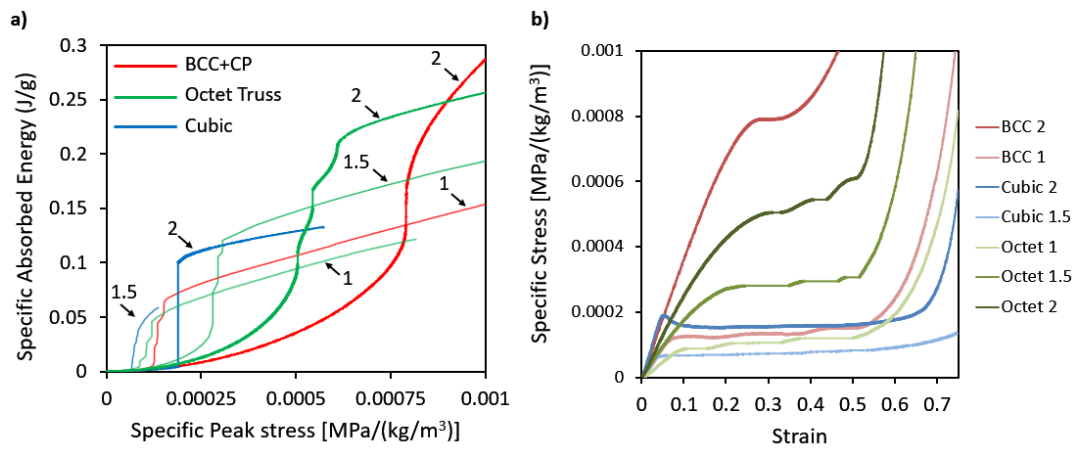


Figure 3.6 (a) Normalized energy diagrams of lattice structures for different types and strut diameters. The number on each curve is the strut diameter of each sample in mm. (b) Normalized compressive stress-strain behavior of the samples investigated in this work.

CHAPTER 4

PART 2: A METHODOLOGY TO DEVELOP METAL-COATED POLYMER LATTICES

4.1 Hybrid Production Process

There are many novel approaches regarding the hybrid production of additive manufacturing processes. Some FFF-based 3D printers can be modified to add layers of certain metallic filaments. Furthermore, the development of composite filaments reinforced with metallic particles can also lead to the production of such multifunctional parts. In this chapter, we combine the excellent 3D printing capabilities of the DLS method with electroless/electroplating, since the RPU 70 is a nonconductive polymer, an electroless coating prior to the main electrolytic plating process is required, to investigate the effects of the addition of metal to a lattice structure on its compressive strength. For this, we selected conventional NiCo as the metal alloy coating material and the well-established honeycomb structure which is printed from rigid polyurethane RPU 70 resin by the Carbon M1 3D printer. Figure 4.1 shows an uncoated honeycomb part next to coated samples after electroplating.



Figure 4.1. Image of a virgin uncoated RPU 70 honeycomb lattice structure next to post-mortem electroplated samples.

4.2 Rigid Polyurethane honeycomb lattice structure

RPU 70 resin is used to print parts for applications that require strength toughness and better heat resistance. The technical data, provided by the vendor, claims that the tensile properties of RPU 70 are as follows. Under tension with 50 mm per minute loading speed in accordance with ASTM D638 Standard Test Method for Tensile Properties of Plastics (D20 Committee 2020) the type I specimens exhibit a tensile modulus of 1700 MPa with a yield strength of 40 MPa at 5% strain and 30% elongation at 40 MPa ultimate tensile strength (UTS)(Carbon 3D Inc. 2020). Figure 4.2 shows the tensile test data taken from the technical datasheet provided by the manufacturer. Furthermore, the glass transition temperature T_g for RPU 70 resin is reported to be 125 C°.

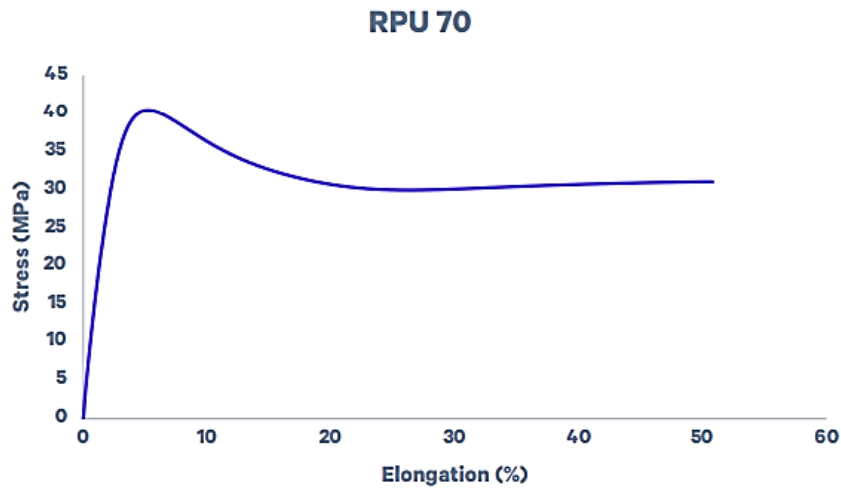


Figure 4.2. Tensile test results of RPU 70 in accordance with ASTM D638 standard with 500 mm/min loading speed.

The RPU 70 based honeycomb structured samples used in this work have been investigated in a recent publication (McGregor, Tawfick, and King 2019a) and were provided to us to use for electroless/electroplating. Figure 4.3(a) shows a top-down view of a unit cell of the honeycomb structure. Figure 4.3(b) shows the CAD image of the part with indications of the important dimensions.

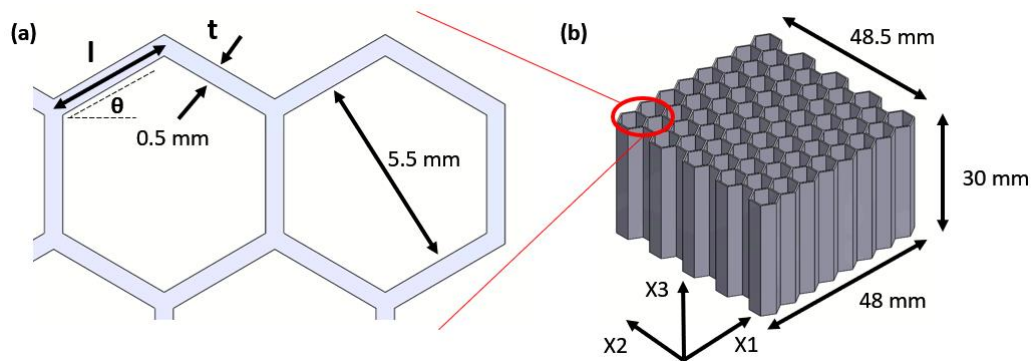


Figure 4.3. (a) A regular hexagonal unit cell of honeycomb structure with a wall thickness of 0.5 mm. (b) Isometric view of the CAD design for the lattice structure with 68 hexagons. The in-plane and out-of-plane directions as well as the overall dimensions of the part are shown in this figure.

The relative density of honeycomb parts can be accurately estimated using the following equation.

$$\bar{\rho} = \left(\frac{t}{l}\right) \frac{3}{2(1 + \sin(\theta)) \cos(\theta)} = \left(\frac{t}{l}\right) 2/\sqrt{3} \quad (23)$$

where t , l , and θ , are the wall thickness, length, and inclination angle (in the case of regular hexagon it is 30°)(L. J. Gibson and Ashby 1997). The relative density of the honeycomb used in this work is calculated to be 23% as the t/l ratio is 0.2.

Honeycomb lattice structures exhibit different mechanical compressive responses depending on the direction of the load. According to the previous work (McGregor, Tawfick, and King 2019a) the honeycomb structure with 23% relative density exhibited a plastic failure with 1.5 ± 0.2 MPa yield strength and 32 ± 12 MPa elastic modulus in the in-plane X2 direction. On the other hand, in the out-of-plane direction the structure exhibited a higher yield strength and elastic modulus, 9.6 ± 0.7 MPa and 180 ± 40 MPa respectively.

4.3 The Electroless Copper Plating process

To deposit Copper on the surface of the polymeric honeycomb parts, first, the parts are cleaned with water and isopropyl alcohol. The excellent surface quality that the DLS method provides, renders the extra surface etching and polishing unnecessary. Next, the part is immersed inside a bath of Copper-salt rich solution with a reduction agent, for a short period of time, in order to create a very thin film of Copper to ensure good surface conductivity for the following process(Garcia et al. 2010;

Bernasconi et al. 2017). The parts are visually inspected and examined by a multimeter to ensure that all the surfaces are covered.

4.4 NiCo Electroplating process

NiCo Electroplating is a relatively time-demanding process and in order to achieve thicker and monotonic deposition, every surface of the part must go through the same conditions (Angel et al. 2018b; Jeon, Yeom, and Oh 2008). Therefore, the anode and cathode placement play a crucial role in the homogeneity and the finished surface quality. In this process, the Copper coated sample acts as the cathode of the electrolytic cell and the anodes are positioned near every surface of the hexagons with a minimum of 1.75 mm distance (Muralidhara and Banerjee 2021). The anodes were circular rods of Ni 201 alloy (over 95% Ni content) with 2 mm diameter. The negative charge on the part was applied by placing the part on a 316L stainless steel sheet with a thickness of 1 mm. The stainless-steel sheet was accurately cut to have the exact same outline and struts of the hexagonal lattice part. To place the anode Ni rods accurately, we designed a setup using SolidWorks v2021 and printed the parts via an Ultimaker 2+, USA, 3D printer with ColorFabb Germany, PLA/PHA filament. Figure 4.4 shows the design and assembly of the setup. The assembly includes 4 supporting parts and a protruded honeycomb block. The holes with 2 mm diameter at the center of each protruded hexagon allowed the Ni rods to pass through and be placed inside every hexagon on the part as well as outside surfaces accurately. The stainless-steel plate is placed on the block and inside the hexagonal pattern

surrounding the protrusions. The Copper plated honeycomb is positioned on top of the SS plate, and firmly held with 4 supporting legs.

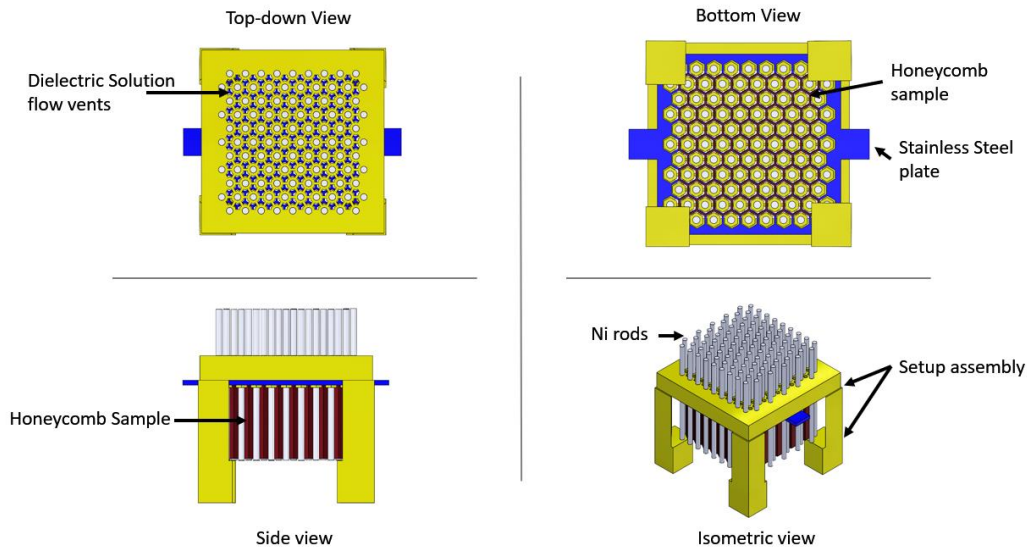


Figure 4.4. Electrolytic unit cell setup. The indicated yellow parts are the setup assembly parts that were 3D printed from PLA/PHA. The blue colored part is the stainless-steel plate that has the accurate hexagonal cutout pattern so it could fit snugly within the spaces between the protrusions.

The Ni rods and SS plate are connected to a power source and the whole setup is submerged inside a dielectric solution bath consisting of Ni and Co salts. A circulating pump was placed under the part to ensure a steady and homogenous flow. The protruded block includes passing through hollow vents to prevent blockage of the flow. The deposition process was repeated after turning the honeycomb structure upside down to ensure no ramping on the deposited coating.

Under steady conditions such as bath temperature (60 degrees), voltage (1V), and flow, the deposition rate stays relatively constant, and the coating thickness depends on the plating duration. Table 4.1 lists the thickness of the coatings on the samples and the corresponding plating duration. The mass of the samples was measured

before and after the plating in order to estimate the thickness of the coatings using according to the overall surface area and density.

Table 4.1. Thickness of the coated samples and the duration of the electroplating process (the electroplating process involved turning the sample inside the setup upside down after half the duration of the coating was reached).

Sample Thickness (μm)	Overall Deposition Duration (minutes)
Uncoated	-
47	90
87	180
97	180

4.5 Coating Thickness

This work, set the target thickness of the coatings to demonstrate a comparable mechanical response to the metallic lattice structure counterparts. Based on the rule of mixture model (Saleh et al. 2004) the resultant elastic modulus and failure stress of the NiCo/RPU composite can be calculated using the following equation.

$$E_{composite} = E_{metal}V_f + E_{polymer}(1 - V_f) \quad (24)$$

Where V_f is the fractional volume of the metallic coating.

Simplified to cross sectional proportion the equation can be modified to just use the coating thickness. By plugging the abovementioned basic assumption into the formulations for honeycomb structures (I. J. Gibson and Ashby 1982) for predicting

the elastic modulus and failure stress, as presented in the following equations, the thickness of the coatings were selected to be in the range of 50 to 100 μm so that the experimental results best showcase their comparable performance.

4.6 Compression test on the coated samples

In the compression test, apparent elastic modulus E^* and yield stress of the samples was compared to the virgin sample with no coating. A Z250 Zwick/Roell, Germany universal testing machine tested the samples in accordance with ASTM D1621-16 (D20 Committee n.d.) in X1 direction. The compression rate was set to a constant 0.00167 S^{-1} strain rate or in other words, 10% of the height of the sample per minute. Figure 4.5 shows the compression test setup. All the tests were recorded using a FujiFilm XS-10 mirrorless camera with a 240p framerate and 1080p resolution.

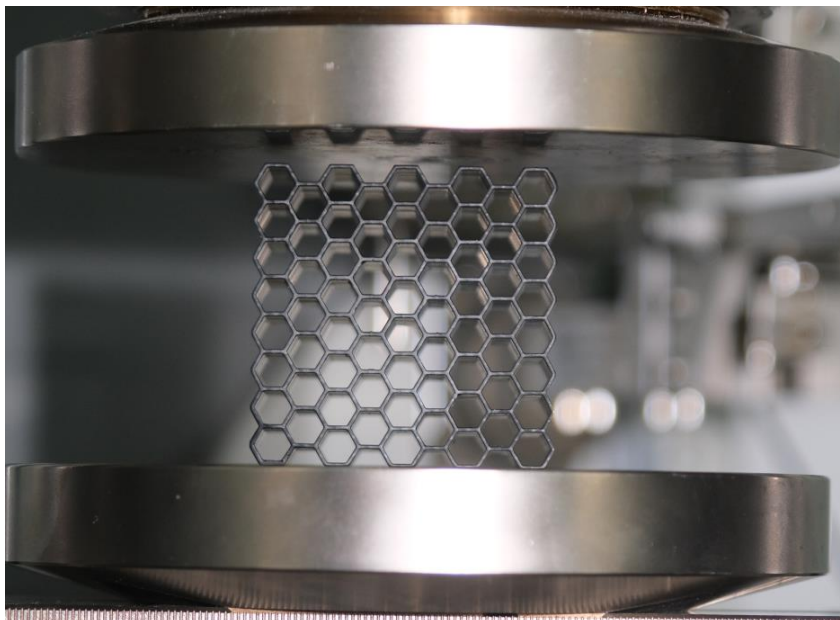


Figure 4.5. Picture taken from the compression test setup.

The samples were placed on top of a rigid plate and compressed against another confronting plate held by a lubricated ball joint to ensure the parallelity of the plates.

Figure 4.6 shows the compression response of the tested samples until yield point. The apparent elastic modulus of the samples was measured using the slope of the near-linear elastic region containing at least 50 data points. Per standard, the yield stress is attributed to the highest exhibited value on the condition that the yield happens before 10% strain which is the case in our samples. Table 4.2 summarizes the results of the tests.

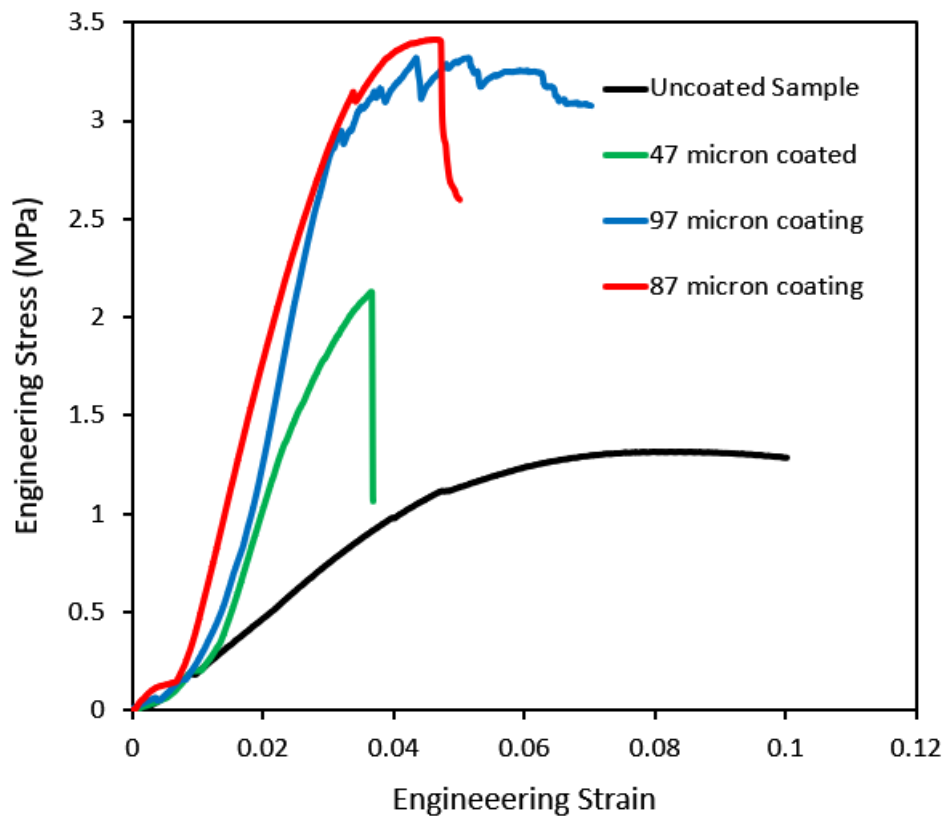


Figure 4.6. Compression test results of coated and uncoated samples up to yield point. Per standard, the yield point is the maximum exhibited stress for the structures that fail within 10% of strain.

Table 4.2. Summary of the compression test results for apparent elastic modulus and yield stress.

Sample	Yield Stress (MPa)	Elastic Modulus (MPa)
Uncoated	1.32	26.2
47 microns coated	2.13	102.78
87 microns Coated	3.41	132
97 microns coated	3.32	156

The uncoated sample exhibited an apparent elastic modulus of 26.2 MPa and yield stress of 1.32 MPa which is on par with the results from the previous work (McGregor, Tawfick, and King 2019a). It is observed that increasing the coating thickness results in a substantially higher modulus and yield stress. The apparent elastic modulus and yield stress of the sample with approximately 47 μm coating were 103 MPa and 2.12 MPa respectively which accounts for a 292.3% and 61% increase. The elastic modulus of the samples with 87 μm and 97 μm coating was 132 MPa and 156 MPa respectively that translates to a 404% and 495% increase when compared to the uncoated honeycomb structure. Furthermore, the yield stresses for the 87 μm and 97 μm samples also increased to 3.41 MPa and 3.32 MPa respectively, accounting for a 159% and 151% increase compared to the virgin sample. Given that to postulate a reliable relationship between coating thickness and increase in strength, a much higher number of repetitions of the tests are required, we cannot confirm such a relationship. However, as demonstrated in Figure 4.7, our test results provide an interesting insight regarding the effect of NiCo coating thickness on the compressive behavior of the polymer lattice structures.

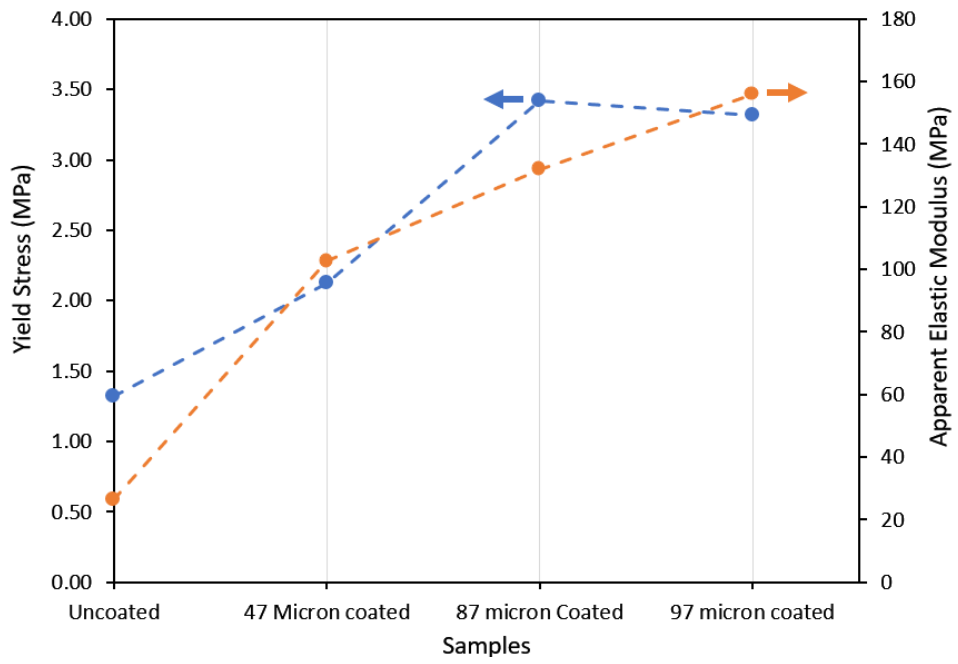


Figure 4.7. summary of the compression test findings that indicate existence of a trend attributed to the thickness of the deposited metal coating.

4.7 Failure mechanism

The test footage indicated a difference between the failure mechanism of the coated and uncoated samples. Figure 4.8 shows snapshots from the footages of the four test samples at the failure point. The uncoated sample, Figure 4.8(a), underwent a plastic failure which includes the collapse of the unit cells on top of the underlying layer coupled with bending and stretching of the struts. This type of failure agrees well with the gradual decrease in stress levels leading to a plateau region until the densification point. The coated samples exhibited a catastrophic failure including delamination and shattering of the coating. As presented in Figure 4.8(b, c, d) the cells start to collapse on a diagonal pattern (shear band). This deformation continues until the cells are fully collapsed as the stress levels decrease. Upon completion of the collapse, the next shear band begins to emerge in opposite direction until densification. We attribute this mechanism to the fact that the metal component provides higher stress capacity before failure at lower strains, however, once the coating fails the underlying polymer fractures due to the orders of magnitude higher stress levels. This failure mechanism does not follow a smooth plateau region, nonetheless, the elevated stress levels indicate that such structures are suitable for high energy impact attenuating applications(Kona et al. 2021; P. Zhang, Arceneaux, and Khattab 2018).

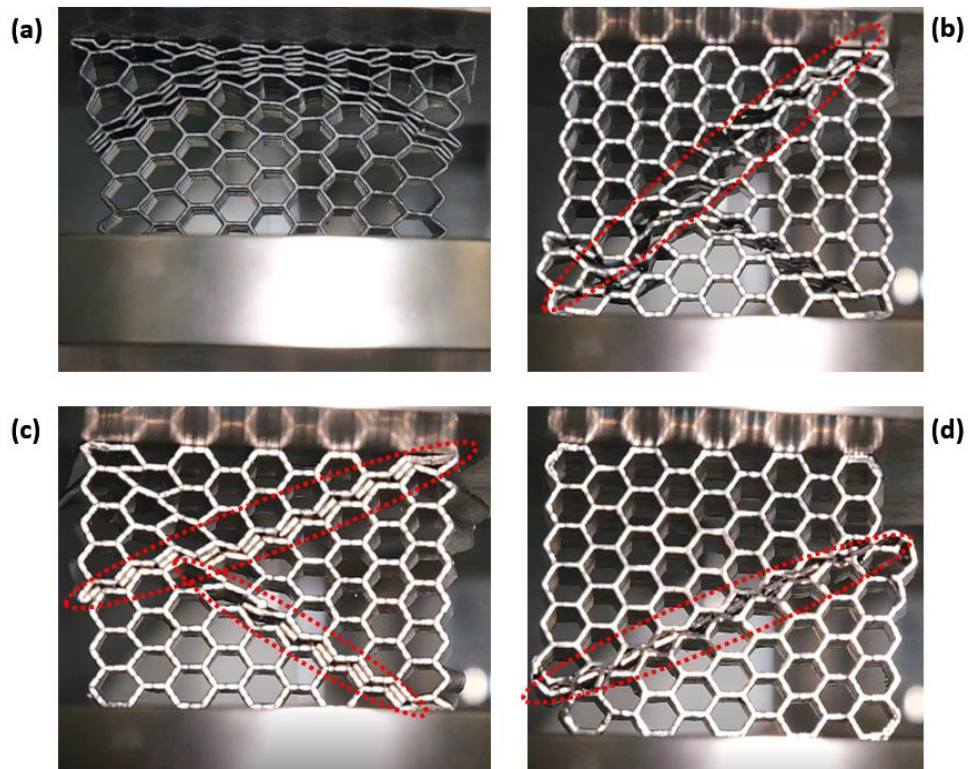


Figure 4.8. Snapshots from the footage of compression tests on (a) uncoated (b) 47 microns coated (c) 97 microns coated and (d) 87 microns coated samples.

CHAPTER 5

CONCLUSIONS AND FUTURE WORK

5.1 Conclusions

This study investigated the mechanical performance of EPU 41 samples produced by Digital Light Synthesis and explored the energy-absorbing behavior of a range of lattice geometries and also investigate a hybrid methodology to produce metalized honeycomb polymeric lattice parts produced by DLS.

Tensile and relaxation testing on EPU 41 showed that the material behaves nonlinear hyperelastic with excellent recovery characteristics. A combination of Ogden model and Prony series successfully described this visco-hyperelastic behavior.

Characterization of a range of lattice structures under compression demonstrated the great potential of the elastomer and the printing approach for the design and implementation of energy-absorbing structures.

In general, Octet-truss structures provide a more reliable and effective architecture for absorbing energy. Accurate control of the slenderness ratio enabled by 3D printing provides means for tuning the peak stress and energy absorbance capacity of this lattice geometry for the requirements of a wide range of applications.

Overall, the excellent printing characteristics of DLS combined with the desirable properties of the hyperelastic elastomer EPU 41 provide a great design space for the development of high-performance energy-absorbing structures.

The hybrid production approach of NiCo coated honeycomb RPU lattice structures lead to an outstanding enhancement regarding the compressive behavior of the polymeric parts. Electroless and subsequent conventional electroplating proved effective in deposition of metallic films on nonconductive polymers.

By preparing and optimizing custom setups for electroplating complex geometries like lattice structures (in the case of this work, honeycomb lattices), effective and high-quality coatings are feasible.

NiCo coated honeycomb structures exhibited three to five folds higher elastic modulus and yield stress which can be suitable for high energy Impact absorbing applications.

5.2 Future work

The desirable results of this study show great potential for further research.

For the case of EPU 41 cubic lattice structures the following in depth analysis can be beneficial:

- Finite element analysis of either single unit cells or the three lattice types studied in this work, will provide deeper insight regarding the deformation behavior of single struts and their critical buckling loads.
- By systematic production of Octet Truss EPU 41 lattice structures and obtaining the envelope of its energy absorbing diagram with regards to

relative density, a useful and comprehensive guide can be prepared for optimal design and production of industry grade parts.

- Combining the viscoelastic dynamic response and hyperelastic results and using the newly developed nonlinear and robust approaches, much more accurate models can be developed that better captures the mechanical properties.

In the case of metallized polymer lattice structures:

- By producing higher quantity of coated samples, the exact effects of coating thickness on the mechanical properties can be confirmed more reliably.
- Micromechanical investigation of the coated metallic alloy through conventional crystallography methods will provide deeper insight regarding the effects of underlying amorphous polymer surface on the overall performance.
- A finite element analysis of the electroplating process through COMSOL Multiphysics program and the investigation of parameters such as charge distribution on the surface of the lattice structure will help to achieve the most optimal plating conditions.

REFERENCES

- Abayazid, Fady F., and Mazdak Ghajari. 2020. "Material Characterisation of Additively Manufactured Elastomers at Different Strain Rates and Build Orientations." *Additive Manufacturing* 33 (May): 101160. <https://doi.org/10.1016/j.addma.2020.101160>.
- Adams, Rhosslyn, Shwe P. Soe, Rafael Santiago, Michael Robinson, Benjamin Hanna, Graham McShane, Marcílio Alves, Roy Burek, and Peter Theobald. 2019. "A Novel Pathway for Efficient Characterisation of Additively Manufactured Thermoplastic Elastomers." *Materials & Design* 180 (October): 107917. <https://doi.org/10.1016/j.matdes.2019.107917>.
- Alghamdi, Ahmad, David Downing, Rance Tino, Abduladheem Almalki, Tobias Maconachie, Bill Lozanovski, Milan Brandt, Ma Qian, and Martin Leary. 2021. "Buckling Phenomena In Am Lattice Strut Elements: A Design Tool Applied To Ti-6AL4V Lb-Pbf." *Materials & Design*, June, 109892. <https://doi.org/10.1016/j.matdes.2021.109892>.
- Angel, Kristin, Harvey H. Tsang, Sarah S. Bedair, Gabriel L. Smith, and Nathan Lazarus. 2018a. "Selective Electroplating of 3D Printed Parts." *Additive Manufacturing* 20 (March): 164–72. <https://doi.org/10.1016/j.addma.2018.01.006>.
- . 2018b. "Selective Electroplating of 3D Printed Parts." *Additive Manufacturing* 20 (March): 164–72. <https://doi.org/10.1016/j.addma.2018.01.006>.
- Arruda, Ellen M., and Mary C. Boyce. 1993. "A Three-Dimensional Constitutive Model for the Large Stretch Behavior of Rubber Elastic Materials." *Journal of the Mechanics and Physics of Solids* 41 (2): 389–412. [https://doi.org/10.1016/0022-5096\(93\)90013-6](https://doi.org/10.1016/0022-5096(93)90013-6).
- Ashby, M.f. 2006. "The Properties of Foams and Lattices." *Philosophical Transactions of the Royal Society A: Mathematical, Physical and Engineering Sciences* 364 (1838): 15–30. <https://doi.org/10.1098/rsta.2005.1678>.

Austermann, Johannes, Alec J. Redmann, Vera Dahmen, Adam L. Quintanilla, Sue J. Mecham, and Tim A. Osswald. 2019. "Fiber-Reinforced Composite Sandwich Structures by Co-Curing with Additive Manufactured Epoxy Lattices." *Journal of Composites Science* 3 (2): 53. <https://doi.org/10.3390/jcs3020053>.

Bagheri, Ali, Irene Buj-Corral, Miquel Ferrer Ballester, Maria Magdalena Pastor, and Francesc Roure Fernandez. 2018. "Determination of the Elasticity Modulus of 3D-Printed Octet-Truss Structures for Use in Porous Prosthesis Implants." *Materials* 11 (12): 2420. <https://doi.org/10.3390/ma11122420>.

Bagheri, Ali, and Jianyong Jin. 2019. "Photopolymerization in 3D Printing." *ACS Applied Polymer Materials* 1 (4): 593–611. <https://doi.org/10.1021/acsapm.8b00165>.

Bakır, A. Alperen, Roozbeh Neshani, and Sezer Özerinç. 2021. "Mechanical Properties of 3D-Printed Elastomers Produced by Fused Deposition Modeling." In *Fused Deposition Modeling Based 3D Printing*, edited by Harshit K. Dave and J. Paulo Davim, 107–30. Materials Forming, Machining and Tribology. Cham: Springer International Publishing. https://doi.org/10.1007/978-3-030-68024-4_6.

Bakır, Ali Alperen, Resul Atik, and Sezer Özerinç. 2021. "Mechanical Properties of Thermoplastic Parts Produced by Fused Deposition Modeling: A Review." *Rapid Prototyping Journal* 27 (3): 537–61. <https://doi.org/10.1108/RPJ-03-2020-0061>.

Bernasconi, R., C. Credi, M. Tironi, M. Levi, and L. Magagnin. 2017. "Electroless Metallization of Stereolithographic Photocurable Resins for 3D Printing of Functional Microdevices." *Journal of The Electrochemical Society* 164 (5): B3059. <https://doi.org/10.1149/2.0081705jes>.

Beyer, Christiane, and Dustin Figueroa. 2016. "Design and Analysis of Lattice Structures for Additive Manufacturing." *Journal of Manufacturing Science and Engineering* 138 (12). <https://doi.org/10.1115/1.4033957>.

Bortoli, Daniel de, Eduardo Mötke Wrubleski, Rogério Marczak, and Jordão Gheller Jr. 2011. *HYPERFIT – CURVE FITTING SOFTWARE FOR*

INCOMPRESSIBLE HYPERELASTIC MATERIAL MODELS.

<https://doi.org/10.13140/2.1.4055.7448>.

Boyce, Mary C., and Ellen M. Arruda. 2000. "Constitutive Models of Rubber Elasticity: A Review." *Rubber Chemistry and Technology* 73 (3): 504–23.

<https://doi.org/10.5254/1.3547602>.

Carbon 3D Inc. 2020. "Carbon-RPU-70-Datasheet-TDS.Pdf." 2020.

<https://3dprinting.com/wp-content/uploads/carbon-RPU-70-datasheet-TDS.pdf>.

"Carbon Design Engine." n.d. Accessed February 1, 2022.

<https://www.carbon3d.com/products/carbon-design-engine/>.

Carbon3D Inc. 2018. "Technical Datasheet for EPU 41."

https://s3.amazonaws.com/carbon-static-assets/downloads/resin_data_sheets/EPU41_TDS.pdf.

Clough, Eric C., Thomas A. Plaisted, Zak C. Eckel, Kenneth Cante, Jacob M. Hundley, and Tobias A. Schaedler. 2019. "Elastomeric Microlattice Impact Attenuators." *Matter* 1 (6): 1519–31. <https://doi.org/10.1016/j.matt.2019.10.004>.

D11 Committee. n.d. "Test Method for Vulcanized Rubber and Thermoplastic Elastomer--Determination of Force Decay (Stress Relaxation) in Compression." ASTM International. Accessed May 21, 2021a. <https://doi.org/10.1520/D6147-97R20>.

———. n.d. "Test Methods for Vulcanized Rubber and Thermoplastic ElastomersTension." ASTM International. Accessed May 21, 2021b. <https://doi.org/10.1520/D0412-16E01>.

D20 Committe. 2020. "Standard Practice for Plastics: Dynamic Mechanical Properties: Determination and Report of Procedures." 2020.

<https://www.astm.org/d4065-20.html>.

D20 Committee. n.d. “Test Method for Compressive Properties of Rigid Cellular Plastics.” ASTM International. Accessed May 21, 2021.
<https://doi.org/10.1520/D1621-16>.

Dal, Hüsnü, Kemal Açıköz, and Yashar Badienia. 2021. “On the Performance of Isotropic Hyperelastic Constitutive Models for Rubber-Like Materials: A State of the Art Review.” *Applied Mechanics Reviews* 73 (2).
<https://doi.org/10.1115/1.4050978>.

Dal, Hüsnü, Yashar Badienia, Kemal Açıköz, and Funda Aksu Denli. 2019. “A Comparative Study on Hyperelastic Constitutive Models on Rubber: State of the Art after 2006.” In *Constitutive Models for Rubber XI*. CRC Press.

Dal, Hüsnü, Osman Gültekin, and Kemal Açıköz. 2020. “An Extended Eight-Chain Model for Hyperelastic and Finite Viscoelastic Response of Rubberlike Materials: Theory, Experiments and Numerical Aspects.” *Journal of the Mechanics and Physics of Solids* 145 (December): 104159.
<https://doi.org/10.1016/j.jmps.2020.104159>.

Davami, Keivan, Mehrdad Mohsenizadeh, Michael Munther, Tyler Palma, Ali Beheshti, and Kasra Momeni. 2019. “Dynamic Energy Absorption Characteristics of Additively-Manufactured Shape-Recovering Lattice Structures.” *Materials Research Express* 6 (4): 045302. <https://doi.org/10.1088/2053-1591/aaf78c>.

Davidson, Jacob D., and N. C. Goulbourne. 2013. “A Nonaffine Network Model for Elastomers Undergoing Finite Deformations.” *Journal of the Mechanics and Physics of Solids* 61 (8): 1784–97. <https://doi.org/10.1016/j.jmps.2013.03.009>.

Diani, Julie, Bruno Fayolle, and Pierre Gilormini. 2009. “A Review on the Mullins Effect.” *European Polymer Journal* 45 (3): 601–12.
<https://doi.org/10.1016/j.eurpolymj.2008.11.017>.

Dilberoglu, Ugur M., Bahar Gharehpapagh, Ulas Yaman, and Melik Dolen. 2017. “The Role of Additive Manufacturing in the Era of Industry 4.0.” *Procedia Manufacturing*, 27th International Conference on Flexible Automation and

- Intelligent Manufacturing, FAIM2017, 27-30 June 2017, Modena, Italy, 11 (January): 545–54. <https://doi.org/10.1016/j.promfg.2017.07.148>.
- Dilibal, Savas, Haydar Sahin, Josiah Owusu Danquah, Md Omar Faruk Emon, and Jae-Won Choi. 2021. “Additively Manufactured Custom Soft Gripper with Embedded Soft Force Sensors for an Industrial Robot.” *International Journal of Precision Engineering and Manufacturing* 22 (4): 709–18. <https://doi.org/10.1007/s12541-021-00479-0>.
- Echeta, Ifeanyichukwu, Xiaobing Feng, Ben Dutton, Richard Leach, and Samanta Piano. 2020. “Review of Defects in Lattice Structures Manufactured by Powder Bed Fusion.” *The International Journal of Advanced Manufacturing Technology* 106 (5): 2649–68. <https://doi.org/10.1007/s00170-019-04753-4>.
- Eßbach, Claudia, Dirk Fischer, and Daniela Nickel. 2021. “Challenges in Electroplating of Additive Manufactured ABS Plastics.” *Journal of Manufacturing Processes* 68 (August): 1378–86. <https://doi.org/10.1016/j.jmapro.2021.06.037>.
- “Fusion 360 with Netfabb.” n.d. Accessed February 1, 2022. <https://www.autodesk.com/products/netfabb/overview>.
- Garcia, Alexandre, Thomas Berthelot, Pascal Viel, Alice Mesnage, Pascale Jégou, Fabien Nekelson, Sébastien Roussel, and Serge Palacin. 2010. “ABS Polymer Electroless Plating through a One-Step Poly(Acrylic Acid) Covalent Grafting.” *ACS Applied Materials & Interfaces* 2 (4): 1177–83. <https://doi.org/10.1021/am1000163>.
- Geterud, Erik G., Pontus Bergmark, and Jian Yang. 2013. “Lightweight Waveguide and Antenna Components Using Plating on Plastics.” In *2013 7th European Conference on Antennas and Propagation (EuCAP)*, 1812–15.
- Gibson, I. J., and Michael Farries Ashby. 1982. “The Mechanics of Three-Dimensional Cellular Materials.” *Proceedings of the Royal Society of London. A. Mathematical and Physical Sciences* 382 (1782): 43–59. <https://doi.org/10.1098/rspa.1982.0088>.

- Gibson, Lorna J., and Michael F. Ashby. 1997. *Cellular Solids: Structure and Properties*. 2nd ed. Cambridge Solid State Science Series. Cambridge: Cambridge University Press. <https://doi.org/10.1017/CBO9781139878326>.
- Ha, Ngoc San, and Guoxing Lu. 2020. "A Review of Recent Research on Bio-Inspired Structures and Materials for Energy Absorption Applications." *Composites Part B: Engineering* 181 (January): 107496. <https://doi.org/10.1016/j.compositesb.2019.107496>.
- Habib, F. N., P. Iovenitti, S. H. Masood, and M. Nikzad. 2017. "In-Plane Energy Absorption Evaluation of 3D Printed Polymeric Honeycombs." *Virtual and Physical Prototyping* 12 (2): 117–31. <https://doi.org/10.1080/17452759.2017.1291354>.
- . 2018a. "Cell Geometry Effect on In-Plane Energy Absorption of Periodic Honeycomb Structures." *The International Journal of Advanced Manufacturing Technology* 94 (5): 2369–80. <https://doi.org/10.1007/s00170-017-1037-z>.
- . 2018b. "Fabrication of Polymeric Lattice Structures for Optimum Energy Absorption Using Multi Jet Fusion Technology." *Materials & Design* 155 (October): 86–98. <https://doi.org/10.1016/j.matdes.2018.05.059>.
- Hanks, Bradley, Joseph Berthel, Mary Frecker, and Timothy W. Simpson. 2020. "Mechanical Properties of Additively Manufactured Metal Lattice Structures: Data Review and Design Interface." *Additive Manufacturing* 35 (October): 101301. <https://doi.org/10.1016/j.addma.2020.101301>.
- Helou, Mark, and Sami Kara. 2018. "Design, Analysis and Manufacturing of Lattice Structures: An Overview." *International Journal of Computer Integrated Manufacturing* 31 (3): 243–61. <https://doi.org/10.1080/0951192X.2017.1407456>.
- Holzappel, Gerhard A. 2002. "Nonlinear Solid Mechanics: A Continuum Approach for Engineering Science." *Meccanica* 37 (4): 489–90. <https://doi.org/10.1023/A:1020843529530>.

Hossain, Mokarram, Rukshan Navaratne, and Djordje Perić. 2020. “3D Printed Elastomeric Polyurethane: Viscoelastic Experimental Characterizations and Constitutive Modelling with Nonlinear Viscosity Functions.” *International Journal of Non-Linear Mechanics* 126 (November): 103546. <https://doi.org/10.1016/j.ijnonlinmec.2020.103546>.

International Seminar: Thermal Analysis and Rheology, Artiaga D??az, Digitalia Ramon, and International Seminar: Thermal Analysis and Rheology Inc. 2005. *Thermal Analysis Fundamentals and Applications to Material Characterization ; Proceedings of the International Seminar--Thermal Analysis and Rheology, Ferrol, Spain, 30 Juny [Sic]-4 July 2003*. A Coru??a, Spain: Universidade da Coru??a, Servizo de Publicaci??ns. <http://www.digitaliapublishing.com/a/1135>.

Jakus, Adam E. 2019. “Chapter 1 - An Introduction to 3D Printing—Past, Present, and Future Promise.” In *3D Printing in Orthopaedic Surgery*, edited by Matthew Dipaola and Felasfa M. Wodajo, 1–15. Elsevier. <https://doi.org/10.1016/B978-0-323-58118-9.00001-4>.

Januszewicz, Rima, John R. Tumbleston, Adam L. Quintanilla, Sue J. Mecham, and Joseph M. DeSimone. 2016. “Layerless Fabrication with Continuous Liquid Interface Production.” *Proceedings of the National Academy of Sciences* 113 (42): 11703–8. <https://doi.org/10.1073/pnas.1605271113>.

Jeon, Jin-Han, Sung-Won Yeom, and Il-Kwon Oh. 2008. “Fabrication and Actuation of Ionic Polymer Metal Composites Patterned by Combining Electroplating with Electroless Plating.” *Composites Part A: Applied Science and Manufacturing*, Fifth Asian–Australian Conference on Composite Materials (ACCM-5), 39 (4): 588–96. <https://doi.org/10.1016/j.compositesa.2007.07.013>.

Jiang, Pan, Zhongying Ji, Changyou Yan, Xiaolong Wang, and Feng Zhou. 2018. “High Compressive Strength Metallic Architectures Prepared via Polyelectrolyte-Brush Assisted Metal Deposition on 3D Printed Lattices.” *Nano-Structures & Nano-Objects* 16 (October): 420–27. <https://doi.org/10.1016/j.nanoso.2017.09.007>.

- Juarez, Theresa, Almut Schroer, Ruth Schwaiger, and Andrea M. Hodge. 2018. "Evaluating Sputter Deposited Metal Coatings on 3D Printed Polymer Micro-Truss Structures." *Materials & Design* 140 (February): 442–50. <https://doi.org/10.1016/j.matdes.2017.12.005>.
- Kona, Srinivas, K. Ch. Sekhar, A. Lakshumu Naidu, and V. V. Rama Reddy. 2021. "Evaluation of Compressive Strength of Thermoplastic Materials Prepared Using 3D Printer with Different In-Fill Structures." In *Advanced Manufacturing Systems and Innovative Product Design*, edited by B. B. V. L. Deepak, D. R. K. Parhi, and B. B. Biswal, 209–15. Lecture Notes in Mechanical Engineering. Singapore: Springer. https://doi.org/10.1007/978-981-15-9853-1_17.
- Kraus, Michael A., Miriam Schuster, Johannes Kuntsche, Geralt Siebert, and Jens Schneider. 2017. "Parameter Identification Methods for Visco- and Hyperelastic Material Models." *Glass Structures & Engineering* 2 (2): 147–67. <https://doi.org/10.1007/s40940-017-0042-9>.
- Ling, Chen, Alessandro Cernicchi, Michael D. Gilchrist, and Philip Cardiff. 2019. "Mechanical Behaviour of Additively-Manufactured Polymeric Octet-Truss Lattice Structures under Quasi-Static and Dynamic Compressive Loading." *Materials & Design* 162 (January): 106–18. <https://doi.org/10.1016/j.matdes.2018.11.035>.
- Liu, Jikai, Andrew T. Gaynor, Shikui Chen, Zhan Kang, Krishnan Suresh, Akihiro Takezawa, Lei Li, et al. 2018. "Current and Future Trends in Topology Optimization for Additive Manufacturing." *Structural and Multidisciplinary Optimization* 57 (6): 2457–83. <https://doi.org/10.1007/s00158-018-1994-3>.
- Mahmoud, Dalia, and Mohamed A. Elbestawi. 2017. "Lattice Structures and Functionally Graded Materials Applications in Additive Manufacturing of Orthopedic Implants: A Review." *Journal of Manufacturing and Materials Processing* 1 (2): 13. <https://doi.org/10.3390/jmmp1020013>.

Maiti, S. K., L. J. Gibson, and M. F. Ashby. 1984. "Deformation and Energy Absorption Diagrams for Cellular Solids." *Acta Metallurgica* 32 (11): 1963–75. [https://doi.org/10.1016/0001-6160\(84\)90177-9](https://doi.org/10.1016/0001-6160(84)90177-9).

McGregor, Davis J., Sameh Tawfick, and William P. King. 2019a. "Mechanical Properties of Hexagonal Lattice Structures Fabricated Using Continuous Liquid Interface Production Additive Manufacturing." *Additive Manufacturing* 25 (January): 10–18. <https://doi.org/10.1016/j.addma.2018.11.002>.

———. 2019b. "Automated Metrology and Geometric Analysis of Additively Manufactured Lattice Structures." *Additive Manufacturing* 28 (August): 535–45. <https://doi.org/10.1016/j.addma.2019.05.026>.

Meem, Asma Ul Hosna, Kyle Rudolph, Allyson Cox, Austin Andwan, Timothy Osborn, and Robert Lowe. 2021. "Impact of Process Parameters on the Tensile Properties of DLP Additively Manufactured ELAST-BLK 10 UV-Curable Elastomer." In . American Society of Mechanical Engineers Digital Collection. <https://doi.org/10.1115/MSEC2021-64002>.

Montgomery, S. Macrae, Xiao Kuang, Connor D. Armstrong, and H. Jerry Qi. 2020. "Recent Advances in Additive Manufacturing of Active Mechanical Metamaterials." *Current Opinion in Solid State and Materials Science* 24 (5): 100869. <https://doi.org/10.1016/j.cossms.2020.100869>.

Moore, Jacob P, and Christopher B Williams. n.d. "FATIGUE CHARACTERIZATION OF 3D PRINTED ELASTOMER MATERIAL," 16.

Muralidhara, H. B., and Soumitra Banerjee. 2021. *3D Printing Technology and Its Diverse Applications*. CRC Press.

Natarajan, Jeyaprakash. 2021. *Advances in Additive Manufacturing Processes*. Bentham Science Publishers.

Nayak, N. C., and D. K. Tripathy. 2002. "Deformation and Energy Absorption Characteristics of Microcellular Ethylene-Octene Copolymer Vulcanizates."

Polymer Engineering & Science 42 (6): 1274–85.

<https://doi.org/10.1002/pen.11030>.

Nazir, Aamer, Kalayu Mekonen Abate, Ajeet Kumar, and Jeng-Ywan Jeng. 2019. “A State-of-the-Art Review on Types, Design, Optimization, and Additive Manufacturing of Cellular Structures.” *The International Journal of Advanced Manufacturing Technology* 104 (9): 3489–3510. <https://doi.org/10.1007/s00170-019-04085-3>.

Ngo, Tuan D., Alireza Kashani, Gabriele Imbalzano, Kate T. Q. Nguyen, and David Hui. 2018. “Additive Manufacturing (3D Printing): A Review of Materials, Methods, Applications and Challenges.” *Composites Part B: Engineering* 143 (June): 172–96. <https://doi.org/10.1016/j.compositesb.2018.02.012>.

“NTop; Next-Generation Engineering Design Software.” n.d. NTopology. Accessed February 1, 2022. <https://ntopology.com/>.

Obadimu, Solomon O., and Kyriakos I. Kourousis. 2021. “Compressive Behaviour of Additively Manufactured Lattice Structures: A Review.” *Aerospace* 8 (8): 207. <https://doi.org/10.3390/aerospace8080207>.

Ogden, Raymond William, and Rodney Hill. 1972. “Large Deformation Isotropic Elasticity – on the Correlation of Theory and Experiment for Incompressible Rubberlike Solids.” *Proceedings of the Royal Society of London. A. Mathematical and Physical Sciences* 326 (1567): 565–84. <https://doi.org/10.1098/rspa.1972.0026>.

Pagac, Marek, Jiri Hajnys, Quoc-Phu Ma, Lukas Jancar, Jan Jansa, Petr Stefek, and Jakub Mesicek. 2021. “A Review of Vat Photopolymerization Technology: Materials, Applications, Challenges, and Future Trends of 3D Printing.” *Polymers* 13 (4): 598. <https://doi.org/10.3390/polym13040598>.

Pan, Chen, Yafeng Han, and Jiping Lu. 2020. “Design and Optimization of Lattice Structures: A Review.” *Applied Sciences* 10 (18): 6374. <https://doi.org/10.3390/app10186374>.

Park, Sang Jin, Tae-Jun Ko, Juil Yoon, Myoung-Woon Moon, Kyu Hwan Oh, and Jun Hyun Han. 2017. "Copper Circuit Patterning on Polymer Using Selective Surface Modification and Electroless Plating." *Applied Surface Science* 396 (February): 1678–84. <https://doi.org/10.1016/j.apsusc.2016.12.007>.

Pelayo, Fernández, David Blanco, Pedro Fernández, Javier González, and Natalia Beltrán. 2021. "Viscoelastic Behaviour of Flexible Thermoplastic Polyurethane Additively Manufactured Parts: Influence of Inner-Structure Design Factors." *Polymers* 13 (14): 2365. <https://doi.org/10.3390/polym13142365>.

Plocher, János, and Ajit Panesar. 2019. "Review on Design and Structural Optimisation in Additive Manufacturing: Towards next-Generation Lightweight Structures." *Materials & Design* 183 (December): 108164. <https://doi.org/10.1016/j.matdes.2019.108164>.

Reppel, Thomas, and Kerstin Weinberg. 2018. "Identification of Hyper- and Viscoelastic Properties of Different Flexible FDM Printed Specimens." *PAMM* 18 (1): e201800382. <https://doi.org/10.1002/pamm.201800382>.

Riva, Leonardo, Paola Serena Ginestra, and Elisabetta Ceretti. 2021. "Mechanical Characterization and Properties of Laser-Based Powder Bed–Fused Lattice Structures: A Review." *The International Journal of Advanced Manufacturing Technology* 113 (3): 649–71. <https://doi.org/10.1007/s00170-021-06631-4>.

Robinson, Michael, Shwe Soe, Richard Johnston, Rhosslyn Adams, Benjamin Hanna, Roy Burek, Graham McShane, Rafael Celeghini, Marcilio Alves, and Peter Theobald. 2019. "Mechanical Characterisation of Additively Manufactured Elastomeric Structures for Variable Strain Rate Applications." *Additive Manufacturing* 27 (May): 398–407. <https://doi.org/10.1016/j.addma.2019.03.022>.

Ruskova, Kamelia, Tsvyatko Pavlov, Boriána Tzaneva, and Peter Petkov. 2018. "Electroless Copper Deposition for Antenna Applications." In *2018 IX National Conference with International Participation (ELECTRONICA)*, 1–4. <https://doi.org/10.1109/ELECTRONICA.2018.8439543>.

Saleh, N., N. Hopkinson, R.J.M. Hague, and S. Wise. 2004. “Effects of Electroplating on the Mechanical Properties of Stereolithography and Laser Sintered Parts.” *Rapid Prototyping Journal* 10 (5): 305–15. <https://doi.org/10.1108/13552540410562340>.

Song, Jian, Libo Gao, Ke Cao, Hongti Zhang, Shang Xu, Chenchen Jiang, James Utama Surjadi, Yiming Xu, and Yang Lu. 2018. “Metal-Coated Hybrid Meso-Lattice Composites and Their Mechanical Characterizations.” *Composite Structures* 203 (November): 750–63. <https://doi.org/10.1016/j.compstruct.2018.07.074>.

Stanković, Tino, and Kristina Shea. 2020. “Investigation of a Voronoi Diagram Representation for the Computational Design of Additively Manufactured Discrete Lattice Structures.” *Journal of Mechanical Design* 142 (11). <https://doi.org/10.1115/1.4046916>.

Tamburrino, Francesco, Serena Graziosi, and Monica Bordegoni. 2018. “The Design Process of Additively Manufactured Mesoscale Lattice Structures: A Review.” *Journal of Computing and Information Science in Engineering* 18 (4). <https://doi.org/10.1115/1.4040131>.

Tengsuwan, Siwach, and Masahiro Ohshima. 2014. “Environmentally Benign Electroless Nickel Plating Using Supercritical Carbon-Dioxide on Hydrophilically Modified Acrylonitrile–Butadiene–Styrene.” *Applied Surface Science* 311 (August): 189–200. <https://doi.org/10.1016/j.apsusc.2014.05.040>.

“The Promise of 3D Printing Fulfilled.” n.d. Carbon. Accessed October 14, 2021. <https://www.carbon3d.com/>.

Thompson, Mary Kathryn, Giovanni Moroni, Tom Vaneker, Georges Fadel, R. Ian Campbell, Ian Gibson, Alain Bernard, et al. 2016. “Design for Additive Manufacturing: Trends, Opportunities, Considerations, and Constraints.” *CIRP Annals* 65 (2): 737–60. <https://doi.org/10.1016/j.cirp.2016.05.004>.

Treloar, L. R. G. 1943. “The Elasticity of a Network of Long-Chain Molecules—II.” *Transactions of the Faraday Society* 39 (0): 241–46.

<https://doi.org/10.1039/TF9433900241>.

Tumbleston, John R., David Shirvanyants, Nikita Ermoshkin, Rima Januszewicz, Ashley R. Johnson, David Kelly, Kai Chen, et al. 2015. “Continuous Liquid Interface Production of 3D Objects.” *Science* 347 (6228): 1349–52.

<https://doi.org/10.1126/science.aaa2397>.

Vaškėlis, A., H. J. Norkus, G. Rozovskis, and H. J. Vinkevičius. 1997. “New Methods of Electroless Plating and Direct Electroplating of Plastics.” *Transactions of the IMF* 75 (1): 1–3. <https://doi.org/10.1080/00202967.1997.11871133>.

Wang, Zenglin, Zhixin Li, Yue He, and Zhixiang Wang. 2011. “Study of an Environmentally Friendly Surface Etching System of ABS for Improving Adhesion of Electroless Cu Film.” *Journal of The Electrochemical Society* 158 (11): D664.

<https://doi.org/10.1149/2.063111jes>.

Xiao, Zefeng, Yongqiang Yang, Ran Xiao, Yuchao Bai, Changhui Song, and Di Wang. 2018. “Evaluation of Topology-Optimized Lattice Structures Manufactured via Selective Laser Melting.” *Materials & Design* 143 (April): 27–37.

<https://doi.org/10.1016/j.matdes.2018.01.023>.

Xu, Fengxiang, Xiong Zhang, and Hui Zhang. 2018. “A Review on Functionally Graded Structures and Materials for Energy Absorption.” *Engineering Structures* 171 (September): 309–25. <https://doi.org/10.1016/j.engstruct.2018.05.094>.

Yabu, Hiroshi, Yuji Hirai, and Masatsugu Shimomura. 2006. “Electroless Plating of Honeycomb and Pincushion Polymer Films Prepared by Self-Organization.” *Langmuir* 22 (23): 9760–64. <https://doi.org/10.1021/la062228r>.

Yaman, Ulas, Melik Dolen, Ugur M. Dilberoglu, and Bahar Gharehpapagh. 2017. “A New Method for Generating Image Projections in DLP-Type 3D Printer Systems.” *Procedia Manufacturing*, 27th International Conference on Flexible

Automation and Intelligent Manufacturing, FAIM2017, 27-30 June 2017, Modena, Italy, 11 (January): 490–500. <https://doi.org/10.1016/j.promfg.2017.07.142>.

Yan, Chunze, Liang Hao, Ahmed Hussein, Simon Lawrence Bubb, Philippe Young, and David Raymont. 2014. “Evaluation of Light-Weight AlSi10Mg Periodic Cellular Lattice Structures Fabricated via Direct Metal Laser Sintering.” *Journal of Materials Processing Technology* 214 (4): 856–64. <https://doi.org/10.1016/j.jmatprotec.2013.12.004>.

Yu, Kunhao, An Xin, Haixu Du, Ying Li, and Qiming Wang. 2019. “Additive Manufacturing of Self-Healing Elastomers.” *NPG Asia Materials* 11 (1): 1–11. <https://doi.org/10.1038/s41427-019-0109-y>.

Zhang, Chi, Fei Chen, Zhifeng Huang, Mingyong Jia, Guiyi Chen, Yongqiang Ye, Yaojun Lin, et al. 2019. “Additive Manufacturing of Functionally Graded Materials: A Review.” *Materials Science and Engineering: A* 764 (September): 138209. <https://doi.org/10.1016/j.msea.2019.138209>.

Zhang, Pengfei, Donald Joseph Arceneaux, and Ahmed Khattab. 2018. “Mechanical Properties of 3D Printed Polycaprolactone Honeycomb Structure.” *Journal of Applied Polymer Science* 135 (12): 46018. <https://doi.org/10.1002/app.46018>.

